Highlights

Robotic Mobile Sensing for Robust Modal Identification across a Population of Bridges: Uncertainty Analysis, Algorithm Development, Hardware Realization, and Field Validation

Xudong Jian,Kiran Bacsa,Matej Varga,Yuguang Fu,Eleni Chatzi

- Uncertainty analysis and evaluation for mobile sensing: This study introduces a theoretical framework clarifying how robot–bridge contact mechanics, sensor deployment, and structural excitation affect vibration measurement uncertainty. The results of the analysis and field tests identify critical scenarios in which uncertainty increases, guiding the optimal robot design and deployment strategies to ensure reliable data for a population of bridges.
- Robust modal identification algorithm: A novel algorithm addresses the time-varying, uncertain nature of mobile sensing data by extracting meaningful vibration modes while quantifying their median frequencies and mode shapes, together with associated standard deviations. This approach enables systematic uncertainty evaluation, meeting the demands of population-based bridge monitoring and advancing reliable, high-quality modal identification from mobile measurements.
- In-the-field hardware validation: Custom-designed, satellite-synchronised mobile sensing devices, including a wheeled robot and a portable sensor box, enable cable-free, rapid field deployment. Validated on ten simply supported bridges, the system demonstrates efficient and scalable data collection while reliably capturing modal parameters and their uncertainties, with proven practical value for population-level assessments supported by finite element analysis comparisons.

Robotic Mobile Sensing for Robust Modal Identification across a Population of Bridges: Uncertainty Analysis, Algorithm Development, Hardware Realization, and Field Validation

Xudong Jian[a,b,*], Kiran Bacsa[a,b], Matej Varga[b], Yuguang Fu[c] and Eleni Chatzi[a,b]

[a] *Future Resilient Systems, Singapore-ETH Centre, Singapore, 138602, Singapore*
[b] *Department of Civil, Environmental and Geomatic Engineering, ETH Zurich, Zurich, 8049, Switzerland*
[c] *School of Civil and Environmental Engineering, Nanyang Technological University, Singapore, 639798, Singapore*

ARTICLE INFO

Keywords:
population-based SHM
robotic mobile sensing
modal identification
uncertainty analysis
vibration measurement
GNSS timing and positioning

ABSTRACT

Population-Based Structural Health Monitoring (PBSHM) has recently emerged as a promising paradigm to enhance monitoring capabilities across populations of structures. A central requirement for PBSHM is the collection of data from different sources. Conventional fixed sensing strategies, whether permanently installed or temporarily deployed, are impractical for this purpose, as they require significant time, labour, and cost. This study introduces a novel robotic mobile sensing framework designed to overcome these challenges. The framework develops a customized portable accelerometer and an intelligent wheeled robot carrying multiple sensors to conduct vibration-based measurements on bridge structures. The collected data enable modal identification, a cornerstone task in PBSHM. To address uncertainties inherent to mobile sensing, we conduct a theoretical uncertainty analysis and develop a robust automated frequency domain decomposition algorithm tailored for mobile data. The proposed framework, which encompasses sensing hardware, uncertainty analysis, and a modal identification algorithm, is validated through field deployment on ten simply supported bridge spans, representative of a bridge population. Using only two sensors, we successfully extract multiple modal frequencies and mode shapes for each span, while quantifying uncertainties in the results. Comparisons with finite element analyses and population-level assessment further confirm the effectiveness of the framework, highlighting its scalability, cost efficiency, and suitability for practical PBSHM implementation.

1. Introduction

Bridge structures are essential components of transportation networks, supporting social mobility, economic development, and public safety. However, over time, they deteriorate due to ageing, harsh environmental conditions, and continuous operational stresses [1]. Without appropriate maintenance, such deterioration can progress to severe damage or even structural failure, as occasionally documented in reported cases. Ensuring timely and cost-efficient maintenance requires structural inspection and monitoring to collect relevant data, followed by robust condition assessment based on these data [2]. Consequently, intensive research over the past few decades has focused on improving the effectiveness and efficiency of bridge inspection, monitoring, and assessment.

An important aspect of research in structural inspection and monitoring is data collection, which includes optimizing sensor deployment as well as developing advanced sensing and data transmission technologies. The overarching goal of these efforts is to enable the collection of richer, higher-quality data with greater operational ease and at lower cost. Representative advances include the use of fibre optic sensors to measure bridge acceleration and strain with high sensitivity, signal-to-noise ratio (SNR), and reliability [3, 4]. Contactless sensing techniques, such as computer vision-based [5] and microwave radar-based approaches [6], have been developed to measure displacement at single or multiple points on a bridge from a distance, as a supplement to conventional acceleration measurements. Additionally, wireless sensors help streamline deployment by removing the need for data transmission cables, thereby reducing both time and labour costs [7]. However, despite these advances, current methods cannot yet fully meet the demands of large-scale bridge inspection and monitoring because they rely on a *fixed sensing scheme* in which

xudong.jian@sec.ethz.ch (X. Jian); chatzi@ibk.baug.ethz.ch (E. Chatzi)
ORCID(s): 0000-0001-9973-9662 (X. Jian); 0000-0002-0834-185X (K. Bacsa); 0000-0002-3453-169X (M. Varga); 0000-0001-7125-0961 (Y. Fu); 0000-0002-6870-240X (E. Chatzi)

the sensor positions are stationary. This requirement renders complete coverage across all bridges in a transportation network prohibitively costly.

To address this challenge, the *mobile sensing scheme* has emerged in recent years, which mounts sensors on mobile platforms such as drones [8, 9, 10], trains [11, 12, 13], cars [14, 15, 16, 17, 18], and robots [19, 20, 21, 22] to perform bridge inspection and monitoring. This approach eliminates the need to install fixed sensor networks on each bridge, offering significant gains in efficiency and reduced cost. Among available platforms, drones offer the greatest mobility and have been widely adopted for large-scale, vision-based bridge inspection [23]. However, vision-based methods are inherently constrained, as various types of structural damage remain invisible on the surface. To capture such hidden defects, vibration-based approaches offer a more promising alternative [24]. Although some research has used drones with computer vision to measure bridge vibration [9], practical deployment remains limited because low-amplitude vibrations of bridges are typically masked by drone jitter. To better capture bridge vibrations, accelerometers have been mounted on trains and cars to indirectly measure bridge response via vehicle-bridge interaction. However, this approach faces major challenges: Vehicle vibrations from road roughness often overwhelm bridge-induced vibrations, and cars and trains themselves are complex dynamic systems [15]. As a result, extracting meaningful structural parameters is rather challenging. In practice, only the first few bridge modal frequencies can be identified [11, 17], which is insufficient for comprehensive evaluation of structural condition. An alternative solution is to use robots for mobile vibration measurement. For example, Zhu et al. [19] developed the flexure-based mobile sensing node (FMSN), a magnetic wall-climbing robot capable of measuring structural acceleration on steel surfaces with wireless data transmission. Using four FMSNs in a "stop-and-go" strategy, they successfully identified the first three high resolution mode shapes of a steel truss footbridge. However, the FMSN is limited to smooth steel surfaces, making it unsuitable for typical concrete bridge decks, and its low speed limits its scalability. Our previous study [20] used a wheeled robot equipped with a wireless accelerometer to measure vibrations on a footbridge, successfully identified the first two modal frequencies and achieved high spatial resolution mode shapes. However, that work did not address the additional uncertainties introduced by mobile sensing and was only validated on a single short-span bridge, leaving its scalability to larger bridge populations untested. In addition, the mobile sensors in that study required synchronization through a dedicated local wireless network, which is impractical for broader field deployments.

Beyond sensing hardware, structural condition assessment is dependent on data processing, which determines how useful the collected measurements become for monitoring and decision making. Data processing methods can be categorized into physics-based and data-driven approaches. In recent years, the data-driven approach has gained traction due to the accumulation of large volumes of bridge inspection and monitoring data and the rapid advancement of powerful machine learning and deep learning tools [25, 26]. Within this data-driven paradigm, an especially notable methodology is Population-Based Structural Health Monitoring (PBSHM). PBSHM represents a paradigm shift in SHM by enabling knowledge transfer across multiple structures within a defined population [27]. Unlike conventional SHM, which analyses each structure independently, PBSHM promotes the sharing of operational and damage-state information, thereby enhancing robustness and cost-effectiveness. Foundational PBSHM research has defined what constitutes a structure population [28] and introduced essential technical tools [29, 30, 31]. Building on this foundation, state-of-the-art PBSHM research has advanced along several key directions, including transfer learning [32], domain adaptation [33, 34], knowledge sharing [35], structural similarity metrics [36], population-based modal identification [37, 38], and damage diagnosis through meta learning [39]. Collectively, these theoretical and simulation-based efforts aim to alleviate data scarcity and pave the way toward scalable monitoring frameworks. Nevertheless, PBSHM remains inherently data-hungry [40], making the collection of real-world datasets from multiple bridge structures within a bridge population indispensable. Without such data, PBSHM research cannot advance effectively toward practical implementation and real-world impact.

Building on the aforementioned studies, this work introduces a novel robotic mobile sensing framework that is robust and scalable, aimed at enabling PBSHM of bridge structures. The main contributions can be summarized as follows:

1) **Uncertainty analysis**. A theoretical framework is developed to investigate how robot–bridge contact mechanics, sensing network configuration, and bridge excitation contribute to uncertainties in computed structural properties, such as modal frequencies and mode shapes, derived from the accelerometer measurements.

2) **Development of robust modal identification algorithm**. To cope with the time-varying characteristics and inherent uncertainties of mobile sensing signals, a robust modal identification algorithm is developed. The algorithm extracts meaningful vibration modes while providing statistical estimates for the corresponding modal frequencies and mode shapes.

3) **Development of hardware**. To support real-world data collection with the proposed robotic mobile sensing approach, two customized sensing devices are developed: a wheeled robot and a portable sensor box, each integrating an accelerometer, a Global Navigation Satellite System (GNSS) module, and a mini-computer.

4) **Field validation with a bridge population**. The proposed approach is validated through field tests on ten simply supported bridge spans, yielding a valuable dataset representative of a bridge population. The results confirm the effectiveness of the uncertainty analysis framework, the robust modal identification algorithm, and the developed sensing hardware.

2. Methodology

[sometimes reviewers ask to have a sentence or two between section and subsection]

2.1. Problem Formulation

The objective of this study is to demonstrate the proposed robotic mobile sensing approach for identifying the modal frequencies and mode shapes of multiple bridges, and to evaluate these results on a population basis. Ideally, the setup employs two portable accelerometers mounted on wheeled robots. The first, termed the *mobile sensor*, moves across the tested bridge using a "stop-and-go" strategy: the robot sequentially halts at predefined locations for a short duration, records data, and then proceeds to the next location until the entire span is covered. The second accelerometer, termed the *reference sensor*, remains fixed at a stationary point on the bridge, serving as a spatial reference for mode shape identification. Crucially, only the vibration data recorded during the stationary intervals of the mobile sensor are used for modal identification. This strategy is specifically adopted to eliminate the effects of robot-induced vibrations caused by road surface roughness, a known limitation in mobile sensing. Under this scheme, if the mobile sensor stops at N locations along the span, the two sensors together yield N pairs of synchronized acceleration signals. The problem of this study can therefore be formulated as:

$$[\mathbf{F}, \mathbf{\Phi}] = \mathcal{M}\left(\begin{bmatrix} \mathbf{a}_m^{(1)} & \mathbf{a}_m^{(2)} & \dots & \mathbf{a}_m^{(N)} \\ \mathbf{a}_r^{(1)} & \mathbf{a}_r^{(2)} & \dots & \mathbf{a}_r^{(N)} \end{bmatrix}\right) \tag{1}$$

where $\mathcal{M}(\cdot)$ denotes the modal identification method. Each pair $\mathbf{a}_m^{(i)} \in \mathbb{R}^{1\times Tf_s}$ and $\mathbf{a}_r^{(i)} \in \mathbb{R}^{1\times Tf_s}$ represents the acceleration signals collected at the i^{th} stop by the mobile and reference sensors, respectively. Here, T is the signal duration (in seconds) and f_s is the sampling frequency (in Hz). The outputs $\mathbf{F} \in \mathbb{R}_{>0}^{1\times P}$ and $\mathbf{\Phi} \in \mathbb{R}^{N\times P}$ denote the identified modal frequencies (in Hz) and the corresponding mode shapes for P structural vibration modes, respectively.

It should be noted that damping identification is not considered in this study. This is because, first, damping ratios are less widely used in practical structural condition assessment compared to modal frequencies and mode shapes. Second, damping is notoriously difficult to estimate accurately, even with fixed sensors rigidly attached to a structure [41]. The robotic mobile sensing setup considered here introduces further complexity: the mobile sensor records bridge accelerations indirectly, with the accelerometer mounted on a robot that rests on the bridge through its self-weight rather than a rigid connection. Intuitively, the robot's mechanical properties, such as its mass, suspension, and contact compliance, may influence the measured signal and thus affect the accuracy of modal identification. Our previous work [20] has demonstrated, through theoretical and experimental analyses, that such influences are negligible provided the robot's modal frequencies do not overlap with those of the bridge. However, that conclusion was derived under a deterministic setting, whereas analysing uncertainty in modal identification is essential [42, 43]. In practice, robotic mobile sensing introduces additional sources of uncertainty, including non-rigid and potentially variable wheel–surface contact, as well as variations in sensing positions across the bridge span.

To quantify and evaluate these uncertainties, this study incorporates both theoretical and data-driven uncertainty analysis. The theoretical analysis is presented in Section 2.2, while the practical evaluation is conducted by applying the robust modal identification algorithm (introduced in Section 2.3) to real-world field data. With uncertainty explicitly considered, the problem defined in Equation (1) is extended as:

$$\left[\bar{\mathbf{F}}, \sigma_{\mathbf{F}}, \bar{\mathbf{\Phi}}, \sigma_{\mathbf{\Phi}}\right] = \mathcal{M}\left(\begin{bmatrix} \mathbf{a}_m^{(1)} & \mathbf{a}_m^{(2)} & \dots & \mathbf{a}_m^{(N)} \\ \mathbf{a}_r^{(1)} & \mathbf{a}_r^{(2)} & \dots & \mathbf{a}_r^{(N)} \end{bmatrix}\right) \tag{2}$$

where $\bar{\mathbf{F}}$ and $\bar{\mathbf{\Phi}}$ represent the median values of identified modal frequencies and mode shapes, respectively, and $\sigma_{\mathbf{F}}$ and $\sigma_{\mathbf{\Phi}}$ denote their corresponding standard deviations.

Equation (2) defines the modal identification task for one bridge span. After inspecting one bridge span, both robots can be easily relocated to the next span, enabling efficient, repeatable, and scalable vibration measurements across a population of bridges.

2.2. Theoretical Analysis

This section presents the theoretical foundations of the proposed robotic mobile sensing approach, with a particular focus on its uncertainty analysis. Figure 1 illustrates the analytical model of the coupled robot-bridge system. The bridge is modelled as an Euler–Bernoulli beam, while each robot is represented as a single-degree-of-freedom (SDOF) sprung mass. As outlined earlier, mobile sensing is carried out using a "stop-and-go" strategy, where only the vibration signals collected while both robots are stationary are considered for analysis. In the configuration shown, the mobile robot (Robot 1) is temporarily positioned at Point 1, whereas the reference robot (Robot 2) remains fixed at Point 2 for the entire measurement duration.

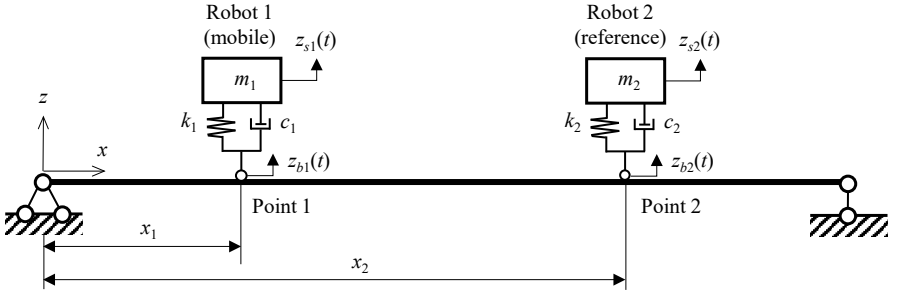

Figure 1: Analytical model of the robot-bridge coupling system. Robots are modelled as SDOF sprung masses and the bridge as an Euler–Bernoulli beam. In this case, the mobile robot (Robot 1) temporarily rests at Point 1, while the reference robot (Robot 2) keeps stationary at Point 2.

In this mobile sensing setup, the robots are significantly lighter than the bridge and, thus, do not influence the vibrational properties of the bridge. The bridge is excited solely by ambient sources, such as traffic and environmental loads. Consequently, the bridge vibrations are independent of the robot dynamics, while the robot vibrations are driven by the bridge response. Based on our previous work [20], the robot acceleration in the frequency domain can be expressed as:

$$\ddot{Z}_{si}(j\omega) = \frac{k_i + j\omega c_i}{k_i + j\omega c_i - m_i\omega^2}\ddot{Z}_{bi}(j\omega) = H_{si}(j\omega)\,\ddot{Z}_{bi}(j\omega), \quad i = 1, 2 \tag{3}$$

where $\ddot{Z}_{si}(j\omega)$ and $\ddot{Z}_{bi}(j\omega)$ denote the acceleration responses of the i^{th} robot and the bridge in the frequency domain, respectively. Here, j is the imaginary unit, m_i is the mass of the i^{th} robot, and k_i and c_i represent the contact stiffness and damping between the robot and the bridge. Moreover, $H_{si}(j\omega)$ denotes the acceleration frequency response function (FRF) of the robot with respect to the ground motion induced by bridge vibration.

Equation (3) illustrates the feasibility of the robotic mobile sensing approach, in which the robots act as dynamic proxies whose vibrations encode information about the bridge. To facilitate the analysis of uncertainties in this approach, Equation (3) is slightly modified as follows:

$$\ddot{Z}_{si}(j\omega) = H_{si}(j\omega)\,\ddot{Z}_{bi}(j\omega) + \eta_i(\omega), \quad i = 1, 2 \tag{4}$$

where $\eta_i(\omega)$ is additive white Gaussian noise with variance $\sigma^2_{\eta_i}$.

Equation (4) suggests three primary sources of uncertainties in the robotic mobile sensing approach: 1) *contact mechanics*, reflected in the frequency response function H_{si}; 2) *time-varying excitation*, included in the bridge response $\ddot{Z}_{bi}$; and 3) *measurement noise*, modelled by η_i.The influence of time-varying excitation is addressed in Subsection 2.3, whereas the present subsection provides the theoretical analysis of uncertainties arising from contact mechanics and measurement noise.

2.2.1. *Uncertainties from the contact mechanics*

Since the robot rests on the bridge solely under its own weight, the values of k_i and c_i in Figure 1 are subject to variability arising from contact mechanics. To represent this uncertainty, k_i and c_i are modeled as jointly normally distributed random variables, expressed as:

$$\begin{bmatrix} k_i \\ c_i \end{bmatrix} \sim \mathcal{N}\left(\begin{bmatrix} \bar{k}_i \\ \bar{c}_i \end{bmatrix}, \begin{bmatrix} \sigma_{k_i}^2 & \mathrm{Cov}(k_i, c_i) \\ \mathrm{Cov}(k_i, c_i) & \sigma_{c_i}^2 \end{bmatrix} \right) = \mathcal{N}\left(\begin{bmatrix} \bar{k}_i \\ \bar{c}_i \end{bmatrix}, \begin{bmatrix} \sigma_{k_i}^2 & \rho\,\sigma_{k_i}\sigma_{c_i} \\ \rho\,\sigma_{k_i}\sigma_{c_i} & \sigma_{c_i}^2 \end{bmatrix} \right) \tag{5}$$

where $\bar{k}_i$ and $\bar{c}_i$ are the mean values of the contact stiffness and damping, respectively, and σ_{k_i} and σ_{c_i} denote their corresponding standard deviations. The term $\mathrm{Cov}(k_i, c_i) = \rho\,\sigma_{k_i}\sigma_{c_i}$ denotes the covariance between k_i and c_i, where ρ is the correlation coefficient. Now we can treat $H_{si}(j\omega)$ as a function of two random variables:

$$H_{si}(j\omega; k_i, c_i) = \frac{j\omega c_i + k_i}{-m_i\omega^2 + j\omega c_i + k_i} \tag{6}$$

As discussed earlier, modal identification in this study is carried out in the frequency domain using the Power Spectral Density (PSD) of vibration signals. Since the PSD is directly proportional to the squared magnitude of the FRF, the uncertainty analysis is conducted on $\left|H_{si}(j\omega; k_i, c_i)\right|^2$ rather than on $H_{si}(j\omega; k_i, c_i)$ itself. This formulation also simplifies the analysis, as $\left|H_{si}(j\omega; k_i, c_i)\right|^2$ is real and non-negative, and can be expressed explicitly as:

$$\left|H_{si}(j\omega; k_i, c_i)\right|^2 = \frac{k_i^2 + \omega^2 c_i^2}{\left(-m_i\omega^2 + k_i\right)^2 + \omega^2 c_i^2}. \tag{7}$$

To estimate the uncertainty in Equation (7), a first-order Taylor expansion is carried out about the mean values $\bar{k}_i$ and $\bar{c}i$ [44], yielding an approximation for the variance of $\left|H si(j\omega; k_i, c_i)\right|^2$ as:

$$\mathrm{Var}\left[|H_{si}|^2\right] \approx \left(\frac{\partial G}{\partial k_i}\right)^2 \sigma_{k_i}^2 + \left(\frac{\partial G}{\partial c_i}\right)^2 \sigma_{c_i}^2 + 2\rho \frac{\partial G}{\partial k_i}\frac{\partial G}{\partial c_i}\sigma_{k_i}\sigma_{c_i}, \tag{8}$$

where $G(k_i, c_i) = |H_{si}(j\omega; k_i, c_i)|^2$.

Let us define:

$$N = k_i^2 + \omega^2 c_i^2, \quad D = \left(-m_i\omega^2 + k_i\right)^2 + \omega^2 c_i^2 \tag{9}$$

and the partial derivatives evaluated at the mean values $\bar{k}_i$ and $\bar{c}_i$ are:

$$\frac{\partial G}{\partial k_i} = \frac{2k_i D - 2N(-m_i\omega^2 + k_i)}{D^2}, \quad \frac{\partial G}{\partial c_i} = \frac{2\omega^2 c_i (D - N)}{D^2} \tag{10}$$

Substituting these expressions into Equation (8) yields the final form:

$$\mathrm{Var}\left[|H_{si}|^2\right] \approx \frac{4}{D^4}\left[\left(k_i D + N(m_i\omega^2 - k_i)\right)^2 \sigma_{k_i}^2 + \omega^4 c_i^2 (D-N)^2 \sigma_{c_i}^2 + 2\rho\omega^2 c_i \left(k_i D + N(m_i\omega^2 - k_i)\right)(D-N)\sigma_{k_i}\sigma_{c_i}\right] \tag{11}$$

Equation (11) shows that the uncertainty in the squared magnitude of the FRF arises from the variances of contact stiffness and damping, as well as their correlation. Importantly, this uncertainty varies with the vibration frequency ω. For example, the denominator term D^4 implies strong sensitivity near resonance, where D is small. the damping-related contribution scales with ω^4, making it dominant at higher frequencies; and the correlation term may either amplify or reduce the overall variance, depending on the sign of ρ.

To illustrate how the frequency ω influences the uncertainty, we use a typical set of mechanical parameters for the robot from our previous study [20], with $m_i = 3$ kg, $\bar{k}_i = 240000$ N/m, and $\bar{c}_i = 50$ N·s/m, to compute the variance. In addition, we specify $\sigma_{k_i} = 24000$ N/m (10% of mean stiffness), $\sigma_{c_i} = 5$ N·s/m (10% of mean damping), and $\rho = -0.5$ (representing a moderate negative correlation consistent with contact mechanics, where stiffer contacts generally exhibit less damping). Based on these settings, the computed $|H_{si}|^2$ and $\mathrm{Var}[|H_{si}|^2]$ are visualized in Figure 2.

Figure 2 illustrates that the uncertainty induced by contact mechanics peaks in the vicinity of the robot's modal frequency, while remaining comparatively small at lower frequencies. This observation suggests that employing a robot with a modal frequency well above the target bridge vibration modes can effectively mitigate uncertainty in robotic mobile sensing.

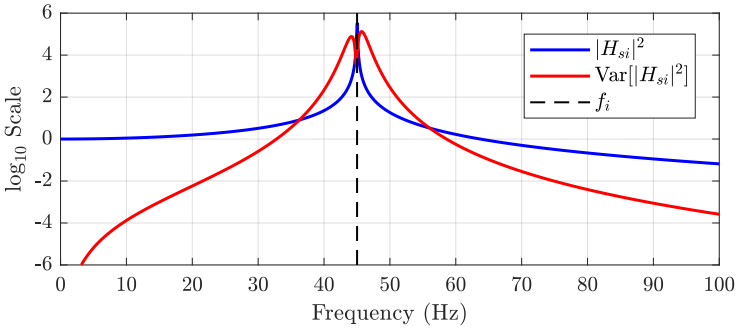

Figure 2: Log_{10} values of the squared magnitude of the FRF $|H_{si}|^2$ and its variance $\text{Var}[|H_{si}|^2]$. The unit of the magnitude is omitted for this qualitative demonstration. The modal frequency of the robot f_i is also indicated.

2.2.2. Uncertainties from the measurement noise

Measurement noise constitutes another important source of uncertainty in the robotic mobile sensing approach. In Equation (4), it is modelled as an additive white Gaussian process $\eta_i(\omega)$ with variance $\sigma^2_{\eta_i}$. Although the "stop-and-go" strategy ensures that the robot remains stationary during measurement, thereby eliminating movement-induced mechanical noise, intrinsic electronic sensor noise remains unavoidable.

To analyse the impact of measurement noise, based on Equation (4), we can mathematically describe the measured acceleration spectrum at the robot location as:

$$|\ddot{Z}_{si}(j\omega)|^2 = |H_{si}(j\omega)|^2\,|\ddot{Z}_{bi}(j\omega)|^2 + |\eta_i(\omega)|^2. \tag{12}$$

Equation (12) shows that the observed PSD is a superposition of the true vibration signal and the noise power. From this relationship, the signal-to-noise ratio (SNR) in robotic mobile sensing can be expressed as:

$$\text{SNR}(\omega) = \frac{|H_{si}(j\omega)|^2\,|\ddot{Z}_{bi}(j\omega)|^2}{\sigma^2_{\eta_i}}. \tag{13}$$

Equation (13) shows that the SNR decreases when the amplitude of the true bridge response $|\ddot{Z}bi(j\omega)|^2$ is low or when the sensor noise variance $\sigma{\eta_i}^2$ is high. A low SNR increases uncertainty in modal identification, as measurement noise may obscure or flatten modal peaks in the PSD, thereby complicating the reliable extraction of modal frequencies and mode shapes in frequency-domain identification.

To mitigate this source of uncertainty in robotic mobile sensing, it is important to employ high-quality accelerometers with low noise floors and to apply suitable signal processing techniques. Nevertheless, there are scenarios where the true bridge response amplitude $|\ddot{Z}_{bi}(j\omega)|^2$ is inevitably low. For example, when the robot is positioned near a bridge support or within frequency bands where traffic loads fail to sufficiently excite the bridge modes, higher identification uncertainty is to be expected in such cases.

2.3. Robust Modal Identification Algorithm

As discussed in Section 2.2, uncertainty in robotic mobile sensing also arises from time-varying excitation, since the approach relies on random traffic loads to excite bridge vibrations. To address this source of uncertainty, together with the effects of contact mechanics and measurement noise analysed above, we develop a robust modal identification algorithm. The pseudocode of this algorithm is presented in Algorithm 1.

As shown in Algorithm 1, the developed robust modal identification algorithm consists of three main blocks:

1) **Modal identification on signal windows.** In this step, short signal windows of length L (with L much smaller than the total signal duration) are extracted from the vibration signals $\mathbf{a}_m^{(i)}$ and $\mathbf{a}_r^{(i)}$ $(i = 1, 2, \ldots, N)$ collected by the mobile and reference sensors. This windowing strategy accounts for the time-varying nature of the vibration response. To capture gradual changes in dynamic characteristics, a sliding-window approach with step size S (where $S \ll L$) is adopted, resulting in overlapping windows. For each window pair, $\mathbf{a}_m^{(i,j)}$ and $\mathbf{a}_r^{(i,j)}$, the Automated Frequency Domain Decomposition (AFDD) method [45], which is an extension of the well-established Frequency Domain Decomposition

Algorithm 1 Robust Modal Identification and Uncertainty Evaluation for Robotic Mobile Sensing

Input: Number of sensing points N; acceleration signals $\mathbf{a}_m^{(i)}$, $\mathbf{a}_r^{(i)}$ $(i = 1, 2, \ldots, N)$; signal window length L (seconds); window step S (seconds); sampling frequency f_s (Hz); number of vibration modes P.
Output: Median and standard deviation of identified modal frequencies $\bar{\mathbf{F}}, \sigma_{\mathbf{F}}$, and mode shapes $\bar{\mathbf{\Phi}}, \sigma_{\mathbf{\Phi}}$.

1. Modal identification on signal windows
Calculate the number of signal windows K based on L, S, and the length of $\mathbf{a}_m^{(i)}$, $\mathbf{a}_r^{(i)}$.
for $i = 1$ to N **do**
    for $j = 1$ to K **do**
        Extract mobile signal window: $\mathbf{a}_m^{(i,j)} = \mathbf{a}_m^{(i)}[(j-1) \cdot S \cdot f_s + (1 : L \cdot f_s)]$
        Extract reference signal window: $\mathbf{a}_r^{(i,j)} = \mathbf{a}_r^{(i)}[(j-1) \cdot S \cdot f_s + (1 : L \cdot f_s)]$
        Apply bandpass filter to $\mathbf{a}_m^{(i,j)}$ and $\mathbf{a}_r^{(i,j)}$.
        Run Automated Frequency Domain Decomposition (AFDD): $[\mathbf{\Phi}^{(i,j)}, \mathbf{F}^{(i,j)}] = \text{AFDD}(\mathbf{a}_m^{(i,j)}, \mathbf{a}_r^{(i,j)})$
    end for
end for

2. K-means clustering
Collect all identified $\mathbf{F}^{(i,j)}$ across K windows and N sensing points.
Perform K-means clustering with $k = P$ to obtain frequency clusters and their indices.
Assign identified mode shapes $\mathbf{\Phi}^{(i,j)}$ to the corresponding frequency clusters to obtain mode shape clusters.

3. Uncertainty evaluation
for each cluster **do**
    Compute median and standard deviation of identified frequencies: $\bar{\mathbf{F}}, \sigma_{\mathbf{F}}$.
    Compute median and standard deviation of identified mode shapes: $\bar{\mathbf{\Phi}}, \sigma_{\mathbf{\Phi}}$.
end for

(FDD) technique [46], is applied to automatically identify the modal frequencies $\mathbf{F}^{(i,j)}$ and mode shapes $\mathbf{\Phi}^{(i,j)}$ of the first P detectable vibration modes. This process is repeated for all K sliding-window pairs obtained from the full signals.

2) **K-means clustering.** Because of the time-varying excitation of bridge vibrations and the automation in AFDD, the sets $\mathbf{F}^{(i,j)}$ may not consistently contain the modal frequencies of the same vibration modes across all windows. For instance, certain modes may not be sufficiently excited by traffic loads in some windows, resulting in missing frequencies in $\mathbf{F}^{(i,j)}$. To identify stable vibration modes, we apply K-means clustering to all collected $\mathbf{F}^{(i,j)}$ with $k = P$. This ensures that frequencies corresponding to stable modes form coherent frequency clusters. The corresponding mode shape clusters are then constructed by assigning the identified mode shapes $\mathbf{\Phi}^{(i,j)}$ to their associated frequency clusters.

3) **Uncertainty evaluation.** After clustering, each frequency and mode shape cluster contains multiple instances corresponding to the same vibration mode. We evaluate the uncertainty of the identified modes by calculating the statistical properties of these clusters. Specifically, the median and standard deviation of the identified modal frequencies and mode shapes are computed within each cluster. These statistical measures constitute the final output of the proposed robust modal identification algorithm, consistent with the problem formulation in Equation (2).

2.4. Integrated Sensing and Identification Framework

This section explains the integrated sensing and identification framework for the proposed robotic mobile sensing approach. The framework is illustrated below.

As shown in Figure 3, the proposed approach consists of two main stages: "stop-and-go" mobile sensing and robust modal identification. In the first stage, bridge vibration signals are collected using custom-developed hardware. In the second stage, these signals are processed to extract modal frequencies and mode shapes, together with their associated standard deviations, thereby enabling both uncertainty quantification and robust modal identification.

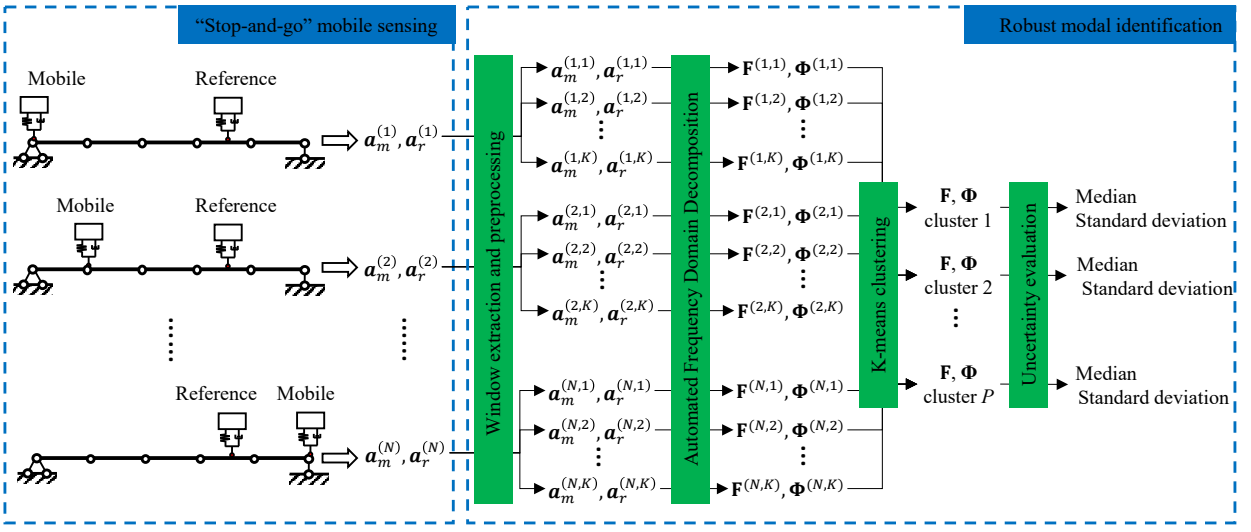

Figure 3: Integrated sensing and identification framework of the proposed robotic mobile sensing approach. The left panel illustrates the "stop-and-go" mobile sensing strategy used for data collection, while the right panel presents the workflow of the proposed robust AFDD algorithm.

3. Field Validation

This section presents field experiments conducted on ten in-service, simply supported, bridge spans. The objective is to understand the following:

1. Can the robotic mobile sensing approach provide an efficient and effective means of measuring bridge vibrations?
2. Can the proposed robust modal identification algorithm reliably identify modal frequencies and mode shapes of the bridges while quantifying their uncertainty?
3. Can the theoretical uncertainty analysis presented in Section 2.2 be validated through field measurements?
4. Does analysing the modal identification results across these ten bridge spans, treated as a population, yield additional insights?

3.1. Sensing Hardware

To implement the proposed robotic mobile sensing approach, customized sensing hardware was developed, consisting of a robotic mobile sensing platform and a portable high-quality accelerometer. An overview of the hardware is provided in Figure 4, with further details described below:

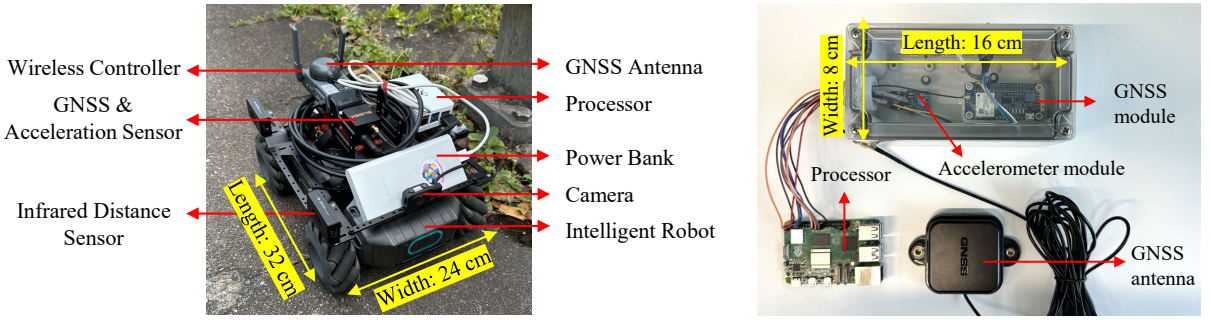

Figure 4: Customized sensing hardware developed for this study: (a) Robotic mobile sensing platform, and (b) Customized Portable Accelerometer.

3.1.1. Robotic Mobile Sensing Platform

As shown in Figure 4(a), the robotic mobile sensing platform was developed using a commercial wheeled robot, the DJI RoboMaster EP. This robot is equipped with four Mecanum wheels, each driven by an individual motor. By independently controlling the speed and direction of each wheel, the robot achieves omnidirectional movement, allowing flexible navigation on bridge surfaces. An onboard inertial measurement unit (IMU) provides measurements of the robot's location and orientation. Both the motors and the IMU are connected to a wireless controller, which communicates via Python scripts running on portable devices such as laptops, tablets, or smartphones, making the robot fully programmable and adaptable. Additional specifications are available on DJI's official website [47].

Although the built-in IMU can measure acceleration, its precision and sampling rate do not meet the requirements of mobile sensing for civil engineering structures. Therefore, in this study a high-quality six-axis accelerometer (Xsens MTi-680G [48]) was mounted on top of the robot. This accelerometer provides a full measurement range of ± 10 g, a -3 dB bandwidth of 500 Hz, and a noise density of 60 $\mu g/\sqrt{Hz}$, making it well suited for measuring bridge vibrations. In addition, the Xsens MTi-680G integrates a GNSS module that supplies satellite-based positioning, navigation, and precise timing signals. This GNSS capability is particularly advantageous: it enables accurate mapping of mode shape measurement locations and ensures precise synchronization between the mobile and reference sensors via GNSS timing, thereby removing the need for a dedicated communication link for clock alignment and enhancing the flexibility of the robotic mobile sensing approach. The Xsens MTi-680G is connected to an onboard processor (Raspberry Pi 5 [49]), which controls the sensor and manages data acquisition and storage.

As shown in Figure 4(a), the RoboMaster EP also supports additional sensors, such as cameras and infrared distance sensors. These extensions could enable autonomous navigation and large-scale bridge inspection in future applications. However, such capabilities are beyond the scope of this paper and are therefore not discussed further.

3.1.2. Customized Portable Accelerometer

In this study, a customized portable sensing box was developed to serve as the reference sensor, which was directly deployed on the bridge surface. As shown in Figure 4(b), the core component of this sensing box is a high-end three-axis accelerometer module, the ADXL355 [50]. The ADXL355 provides an ultra-low noise density of 22.5 $\mu g/\sqrt{Hz}$, a full measurement range of ± 8 g, and a -3 dB bandwidth of approximately 1500 Hz, making it well suited for measuring bridge vibrations. In addition, a high-quality GNSS module (ZED-F9P [51]) is integrated to provide satellite-based positioning and precise timing signals. The ZED-F9P, also employed in the Xsens MTi-680G described above, features a multi-band radio-frequency front-end architecture capable of concurrently receiving all four major GNSS constellations (GPS, GLONASS, Galileo, and BeiDou), thereby significantly enhancing positioning and timing accuracy. Both the ADXL355 and ZED-F9P are connected to a processor (Raspberry Pi 5 [49]), which controls the sensing modules and manages data acquisition and storage.

It is important to note that in this study the reference sensor was not mounted on a second robot. Ideally, the proposed robotic mobile sensing approach would be implemented using two robots, each equipped with sensors. However, our previous work [20] has demonstrated that it remains feasible to employ one mobile sensor mounted on a robot in combination with a reference sensor fixed directly to the bridge surface for modal identification. For research purposes, this configuration is particularly valuable, as it allows direct comparison between the indirect measurements obtained from the robot-mounted sensor and the direct measurements from the fixed reference sensor, thereby providing additional insights into the performance of the robotic mobile sensing approach. Nonetheless, for future applications it is recommended that the reference sensor also be mounted on a second robot. Such a strategy would not only improve modal identification performance (as shown in our previous work [20]), but also enhance mobility, enabling two robots to efficiently traverse and inspect multiple bridges.

3.2. Tested Bridge Spans and Test Setup

The bridge selected for field validation is a flyover crossing an expressway in Singapore. This flyover is located on a main road leading to the busy Port of Singapore, resulting in frequent passage of container trucks that provide ample dynamic excitation to the bridge structure. The flyover comprises a total of 15 simply supported spans, of which 10 were selected for field testing to serve as a representative sample of the entire bridge population. Additional details about the tested spans and the experimental setup are shown in Figure 5.

Figure 5(a) shows a top view of the 10 tested bridge spans, divided into two parallel groups: the east group and the west group. Each group consists of five simply supported spans, numbered E1-E5 and W1-W5. Spans in corresponding pairs (e.g., E1 and W1) have the same approximate length, which is around 30, 31, 39, 36, and 30 meters for spans

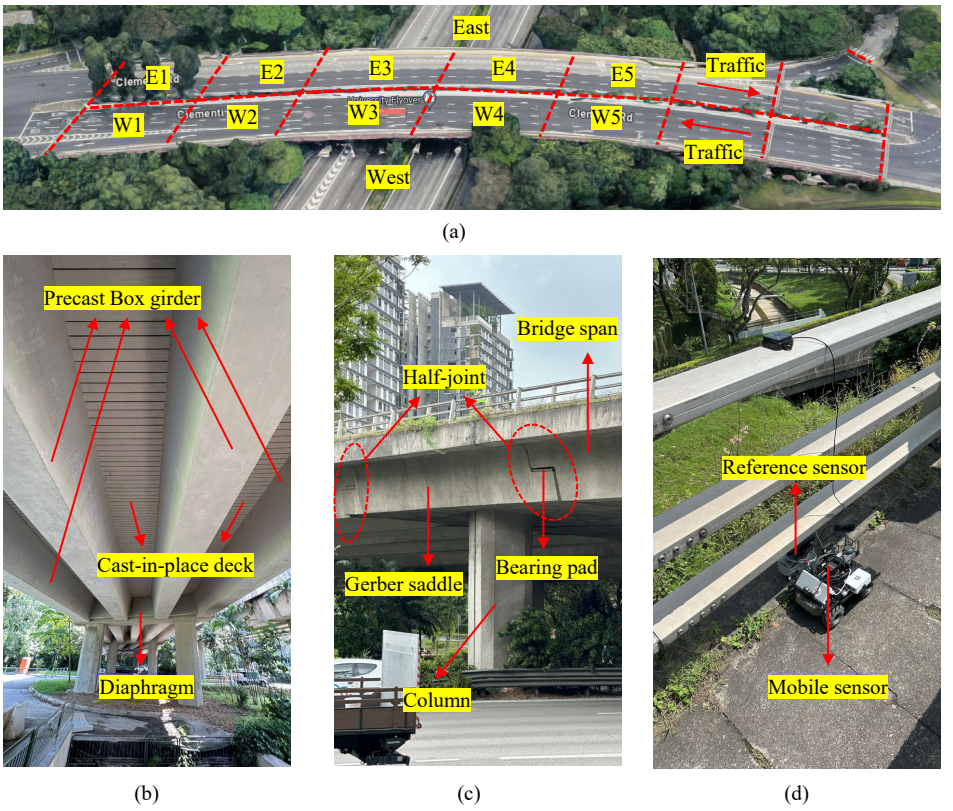

Figure 5: Photos of tested bridge spans and test setup: (a) Top view, with tested bridge spans on the east and west sides labelled E1-E5 and W1-W5; (b) Bottom view, showing the structural type as a multi-girder box bridge; (c) Side view, illustrating the simply supported boundary conditions; (d) Sensor deployment on the bridge, with both sensors deployed on the footpath.

1 through 5, respectively (precise lengths cannot be disclosed due to confidentiality requirements). The east and west groups are structurally separate, with one-way traffic on each side, ensuring that each span is structurally independent. Furthermore, all 10 tested spans share the same structural type and material properties, making them a valuable heterogeneous set for research on robotic mobile sensing and population-based structural health monitoring.

Figure 5(b) shows the bottom view of the tested spans. From this perspective, it is evident that the superstructure consists of multiple precast box girders supporting a cast-in-place concrete deck. Specifically, spans 1, 2, 3, 4, and 5 contain 5, 4, 5, 4, and 5 box girders, respectively, thereby contributing to the diversity of the bridge population. Diaphragms are constructed at both ends of each span to improve structural integrity.

Figure 5(c) shows the side view of the tested spans. A typical Gerber saddle can be observed in the photo, confirming the presence of internal hinges that render each span structurally simply supported in the longitudinal direction. Although the cast-in-place deck slab appears continuous across multiple spans, the Gerber saddle hinges are intentionally designed to release moments, thereby preventing longitudinal moment continuity between adjacent spans. Consequently, each span behaves as an independent simply supported unit for structural analysis, while the continuous deck slab simultaneously provides transverse load distribution and structural unification.

Figure 5(d) illustrates the sensor deployment. Because traffic on the bridge could not be interrupted, both sensors were placed on the footpath and operated at a sampling frequency of 100 Hz. The reference sensor was positioned near the quarter-span of each bridge span and fixed directly to the bridge surface using removable adhesive. The mobile sensor, mounted on the RoboMaster EP platform, traversed the footpath in a “stop-and-go” manner. At each sensing position, the mobile sensor recorded acceleration data for 4 minutes, providing a balance between sensing efficiency and the accuracy of modal identification. The distance between adjacent sensing positions was approximately 6 meters.

As a result, data collection for a single bridge span required about 30 minutes, after which both sensors were redeployed to the next span.

To further illustrate the steps of the "stop-and-go" strategy, Figure 6 shows the satellite-based positioning results for both sensors across all 10 tested bridge spans, including their moving paths and measurement stops. The satellite map confirms that the recorded positions align well with the pedestrian walkway along both edges of the tested flyover, demonstrating high positioning accuracy. This precise positioning is crucial for mode shape identification, which relies on knowing the exact sensor locations. In addition to positioning, satellite signals were also used for signal synchronization. Notably, the two sensors were not synchronized during data collection. Instead, synchronization was performed during post-processing using precise satellite clock timestamps. This strategy substantially reduces deployment time and cost compared to conventional bridge vibration testing, as it requires only two sensors and eliminates the need for cables or on-site communication for data transfer and synchronization.

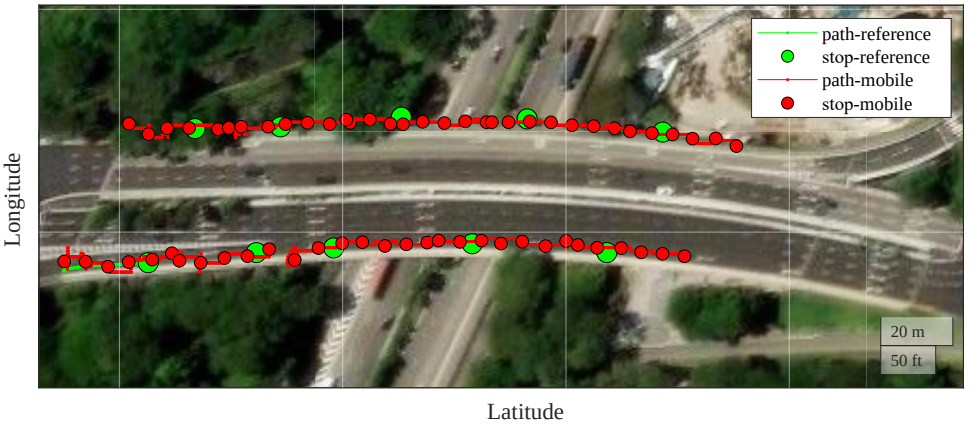

Figure 6: Satellite-based positioning results of the two sensors for the mobile sensing campaign on all 10 tested bridge spans. The moving paths of the reference sensor and mobile sensor are shown in green and red lines, respectively. The position of the stops when the sensors are stationary are marked with green and red dots, respectively.

3.3. Experimental Results

3.3.1. Data Preprocessing

Before conducting modal identification, data preprocessing is essential not only to synchronize the vibration acceleration signals, but also to filter out unwanted disturbances and frequency components. To illustrate the need for preprocessing, Figure 7 and Figure 8 show the raw vibration signals collected by both sensors from bridge spans E5 and W5, respectively.

Figures 7 and 8 highltight several important observations:

1) **Time-varying nature**: As discussed earlier, the tested bridge spans are primarily excited by random traffic loads, particularly heavy container trucks. This is evident in the time-history signals in Figures 7(a) and 8(a), where signal amplitudes increase significantly during truck passages. The PSD plots in Figures 7(b) and 8(b) further show that the frequency content varies across sensing stops, underscoring the time-varying nature of the excitation. This necessitates the use of the proposed robust modal identification algorithm.

2) **Frequency-domain characteristics**: In the frequency band of [3, 20] Hz, the PSDs of the mobile and reference sensors exhibit common peaks with comparable magnitudes, demonstrating effective transmission of bridge vibrations to the robot-mounted sensor. Below 3 Hz, the spans display low vibration energy, which is expected for medium-span bridges whose first modal frequencies typically exceed 3 Hz. In this range, the robot shows notable energy likely caused by micro-slipping on the bridge surface. Above 20 Hz, the mobile sensor's PSD magnitude greatly exceeds that of the reference sensor, since higher-order bridge modes are difficult to excite under normal traffic, whereas the robot has high internal modal frequencies and its motors emit high-frequency vibrations even when stationary. Notably, both Figures 7(b) and 8(b) display a distinct peak near 42 Hz in the mobile sensor's PSD, absent from the reference sensor, suggesting a robot modal frequency around 42 Hz.

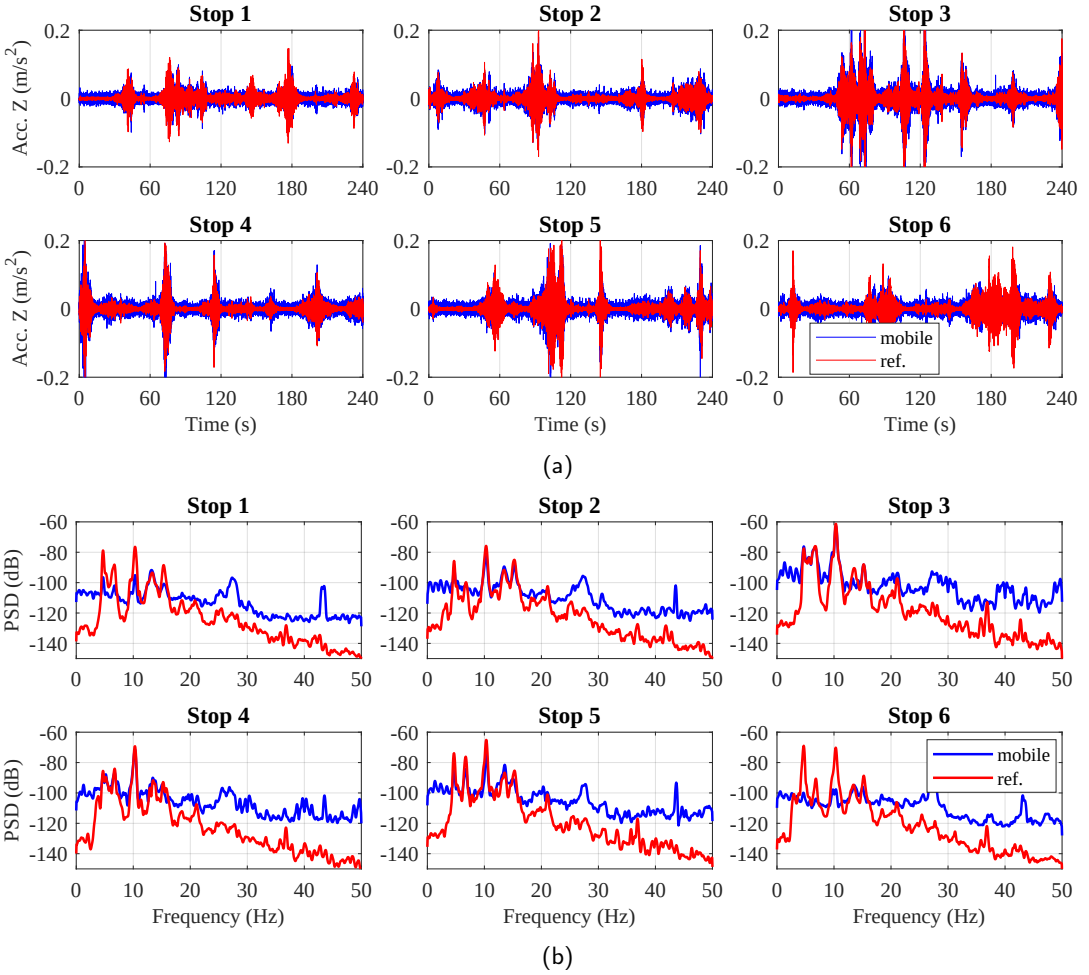

Figure 7: Raw vibration acceleration signals of bridge span E5, collected using the "stop-and-go" strategy. Signals recorded by the mobile sensor mounted on the robot are shown in blue, while those recorded by the reference sensor fixed on the bridge are shown in red: (a) Time-history signals from six stops; (b) Corresponding PSD of (a).

3) **Unwanted disturbances**: In Figure 8(a), distinct spikes appear in the mobile sensor data at Stops 1, 2, and 6, which are absent from the reference sensor. These disturbances are likely caused by external effects, such as pedestrians accidentally touching the robot or sudden slips due to the bridge slope. Since these artifacts do not originate from bridge vibrations, they must be removed to ensure high-quality modal identification.

4) **Magnitude differences between spans**: The signal magnitude from Span W5 is noticeably smaller than that from Span E5, a trend observed across other spans as well. This difference arises because more container trucks travel eastbound toward the Port of Singapore, providing stronger dynamic excitation on the east side of the flyover. Conversely, westbound trucks often enter the expressway before the flyover, leading to weaker traffic-induced loads. As shown in the theoretical analysis (Section 2.2) and later confirmed in the field evaluation of uncertainty (Section 3.3.2), the intensity of these traffic loads directly influences the uncertainty of modal analysis.

Based on the observations of the raw signals, a two-step filtering approach is employed for preprocessing. First, a time-domain Hampel filter is applied to the raw acceleration signals to remove unwanted disturbances. The Hampel filter [52] is a robust outlier detection method that uses the median and median absolute deviation within a sliding window to identify and replace impulsive noise or spikes, while preserving the underlying signal trends. Second, a bandpass filter is applied to the Hampel-processed signals to eliminate unwanted frequency components. Since this study adopts these standard filtering techniques without further modification, detailed technical derivations are omitted. For implementation, the `hampel` and `bandpass` functions available in MATLAB R2024b [53] are used. The `hampel`

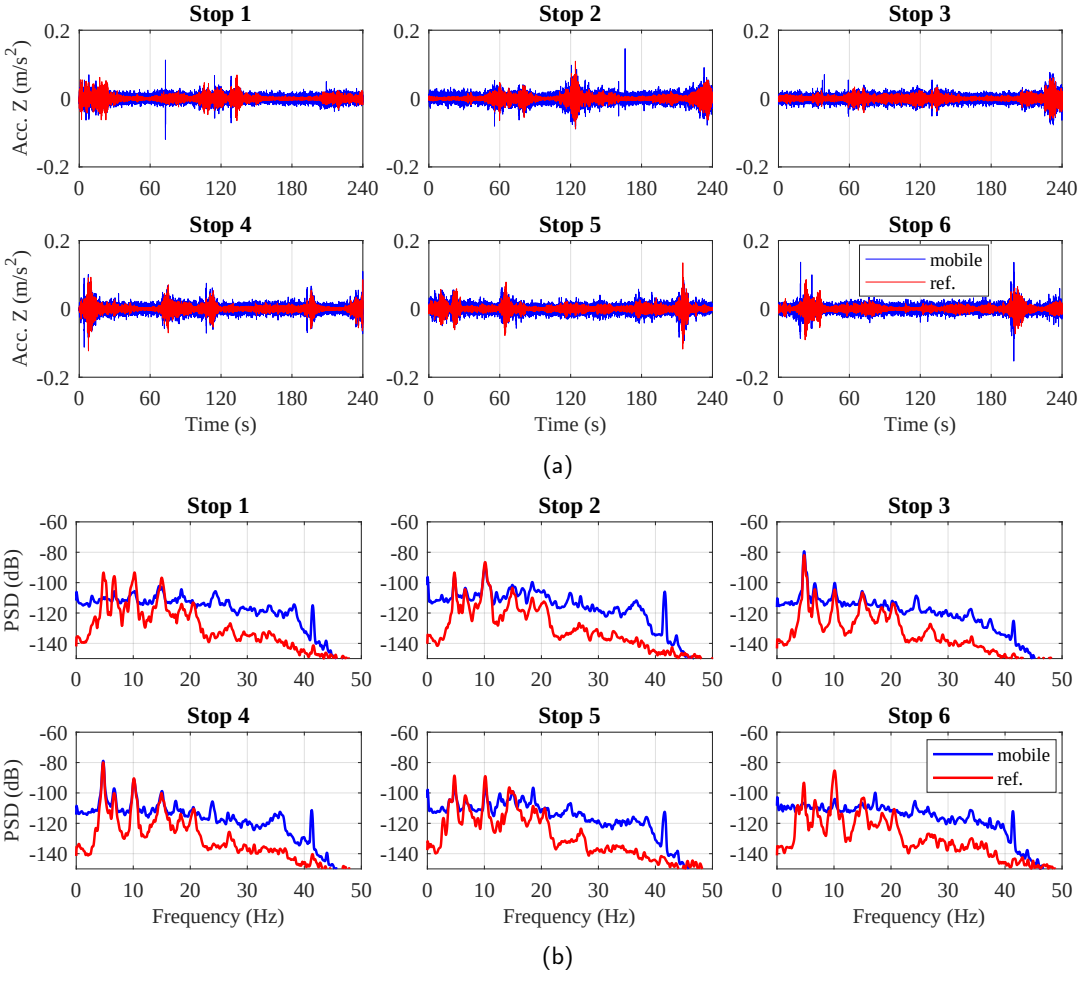

Figure 8: Raw vibration acceleration signals of bridge span W5, collected using the "stop-and-go" strategy. Signals recorded by the mobile sensor mounted on the robot are shown in blue, while those recorded by the reference sensor fixed on the bridge are shown in red: (a) Time-history signals from six stops; (b) Corresponding PSD of (a).

function is configured with a sliding window length of 100 data points and a threshold of three standard deviations for outlier detection. The `bandpass` function is configured with a passband frequency range of [3, 20] Hz and a transition band steepness of 0.99.

To illustrate the effect of preprocessing, Figure 9 presents the processed acceleration signals from bridge span W5 together with their corresponding PSDs. A comparison of the time-history signals in Figure 8(a) and Figure 9(a) shows that the Hampel filter effectively removes unwanted spikes from the mobile sensor data while preserving the underlying vibration waveforms. Similarly, a comparison of the PSDs in Figure 8(b) and Figure 9(b) demonstrates that the bandpass filter successfully eliminates frequency components outside the [3, 20] Hz passband range.

3.3.2. Robust Modal Identification

In this section, we present the modal identification results derived from the preprocessed vibration acceleration signals using the proposed robust modal identification algorithm. The algorithm is implemented with a window length of 60 seconds, a window step of 5 seconds, and is configured to identify 12 vibration modes. A comparative study to determine the optimal algorithm settings is beyond the scope of this paper and is therefore not included for brevity. However, we plan to make our code and sample data publicly available on GitHub [54] upon publication of this paper, enabling interested readers to conduct their own sensitivity analyses on algorithm parameters.

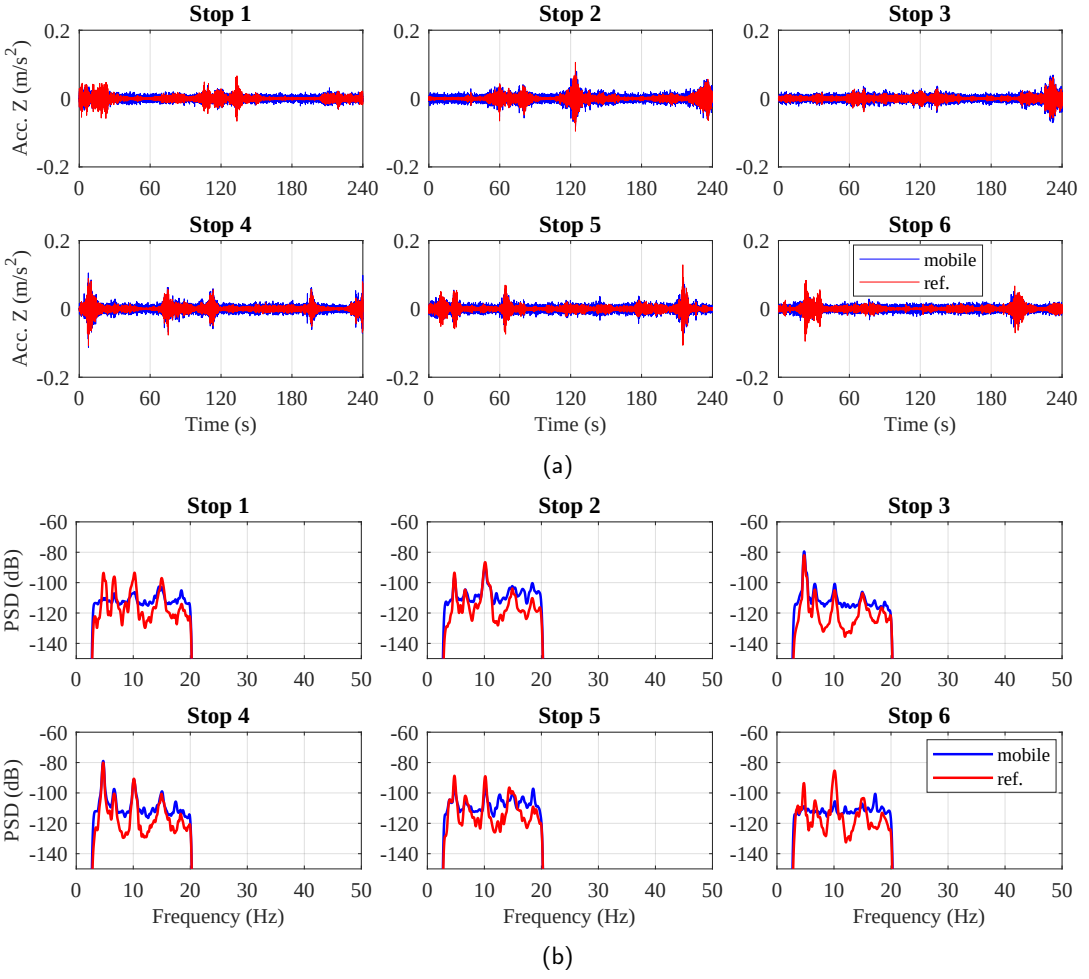

Figure 9: Vibration acceleration signals of bridge span W5, preprocessed by Hampel filter and bandpass filter. Signals recorded by the mobile sensor mounted on the robot are shown in blue, while those recorded by the reference sensor fixed on the bridge are shown in red: (a) Time-history signals from six stops; (b) Corresponding PSD of (a).

Due to space constraints, we focus here on detailed results for two representative bridge spans (E5 and W5), whose measurements were described earlier in Section 3.3.1. Summary results for all 10 tested bridge spans will be presented in the population-level assessment in Section 3.3.3. The modal identification results for bridge spans E5 and W5 are shown in Figure 10 and Figure 11, leading to the following observations:

1) Figure 10(a) and Figure 11(a) highlight the time-varying nature of the vibration acceleration signals, as the identified frequencies differ across individual signal windows. Several frequencies occur only intermittently, leading to uncertainty in frequency identification. In contrast, certain frequencies are detected consistently across nearly all windows, indicating that they correspond to the true vibration modes of the tested bridge spans.

2) Figure 10(b) and Figure 11(b) visualize the statistical properties of the identified frequency clusters. In general, the more stable a cluster is (i.e., the lower its variance), the more likely it corresponds to a true bridge vibration mode, thereby supporting robust modal identification. It is also observed that high-frequency clusters tend to exhibit larger variances than low-frequency clusters. This finding is consistent with the theoretical analysis in Section 2.2, which predicts increasing uncertainty as the frequency approaches the robot's modal frequency (approximately 42 Hz in this study).

3) Figure 10(c) and Figure 11(c) present the median values and standard deviations of the identified frequencies and mode shapes. Several meaningful mode shapes are successfully identified, including modes 2, 3, 5, and 7 for span E5, and modes 2, 3, 5, 11, and 16 for span W5. These shapes exhibit sinusoidal-like patterns typical of the vibration modes

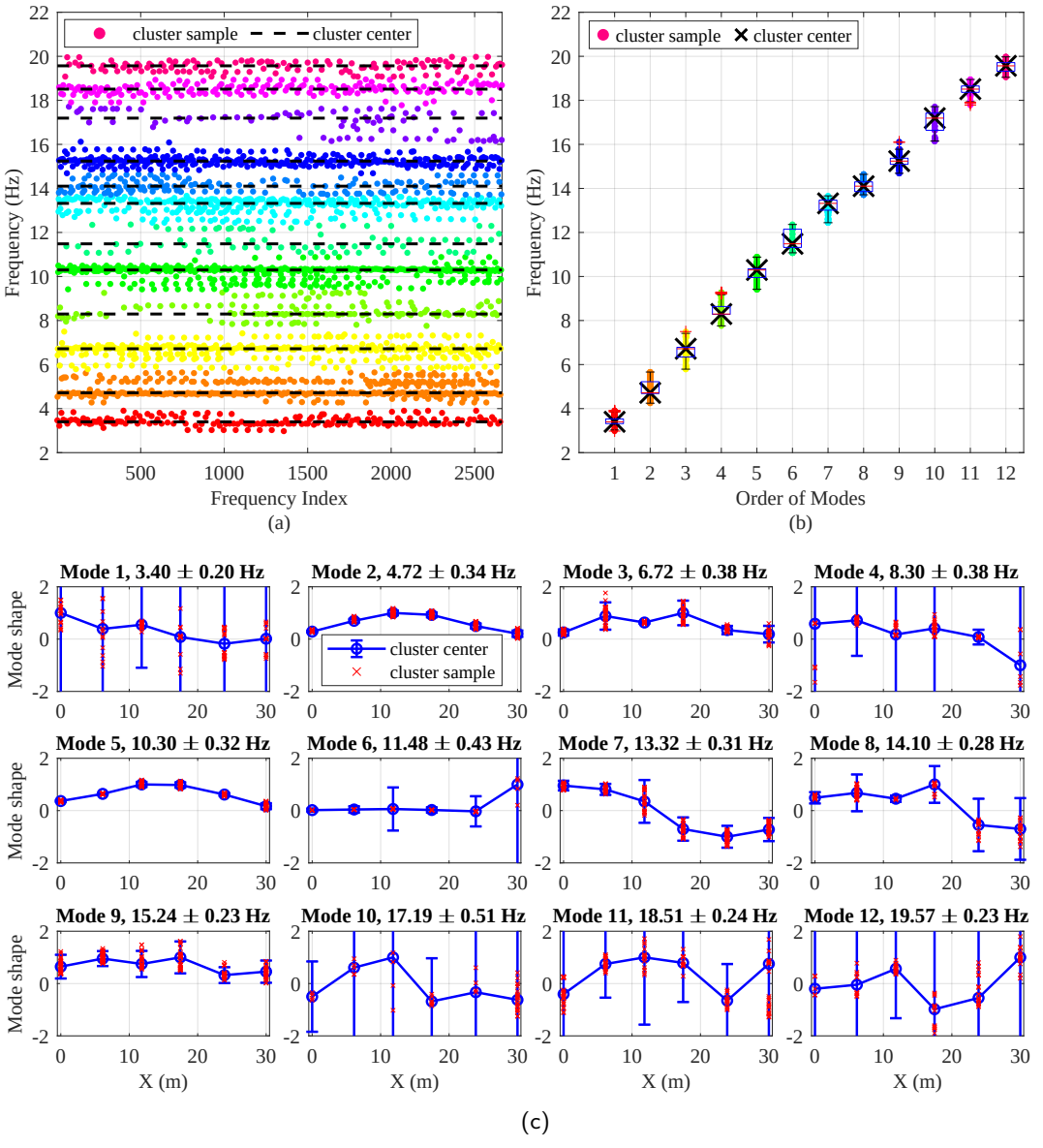

Figure 10: Robust modal identification results for tested bridge span E5: (a) Frequency identification results shown as clusters of frequencies identified from all signal windows. Different clusters are distinguished by colour, with each dot representing a frequency identified from a single signal window. Cluster centres, indicated by dashed lines, represent the median values of the identified frequencies; (b) Box plot of the frequency clusters in (a), used to visualize uncertainty. The median and standard deviation of each frequency cluster is presented in titles of (c); (c) Normalized mode shape identification results. Each red cross indicates the mode shape ratio identified from a single signal window, but some of them exceed the plotting range and are not fully displayed. Crosses are grouped by mode order and sensing location, based on their associated frequencies and satellite-based positioning. The median value of the mode shape ratio clusters at each location is connected by blue lines to visualize the identified mode shapes, with error bars denoting the standard deviation.

of simply supported bridges. The consistency of the identified frequencies for the corresponding modes between the E5 and W5 spans further supports their interpretation as bridge vibration modes. For example, mode 2 in both spans has nearly identical frequencies, which is expected given that E5 and W5 share the same structural type and dimensions. Importantly, the error bars indicate that the variance of the identified mode shapes tends to increase with mode order (e.g., modes 9 and 11 in span W5) and near the bridge supports (e.g., modes 2 and 3 in span W5). This trend is consistent

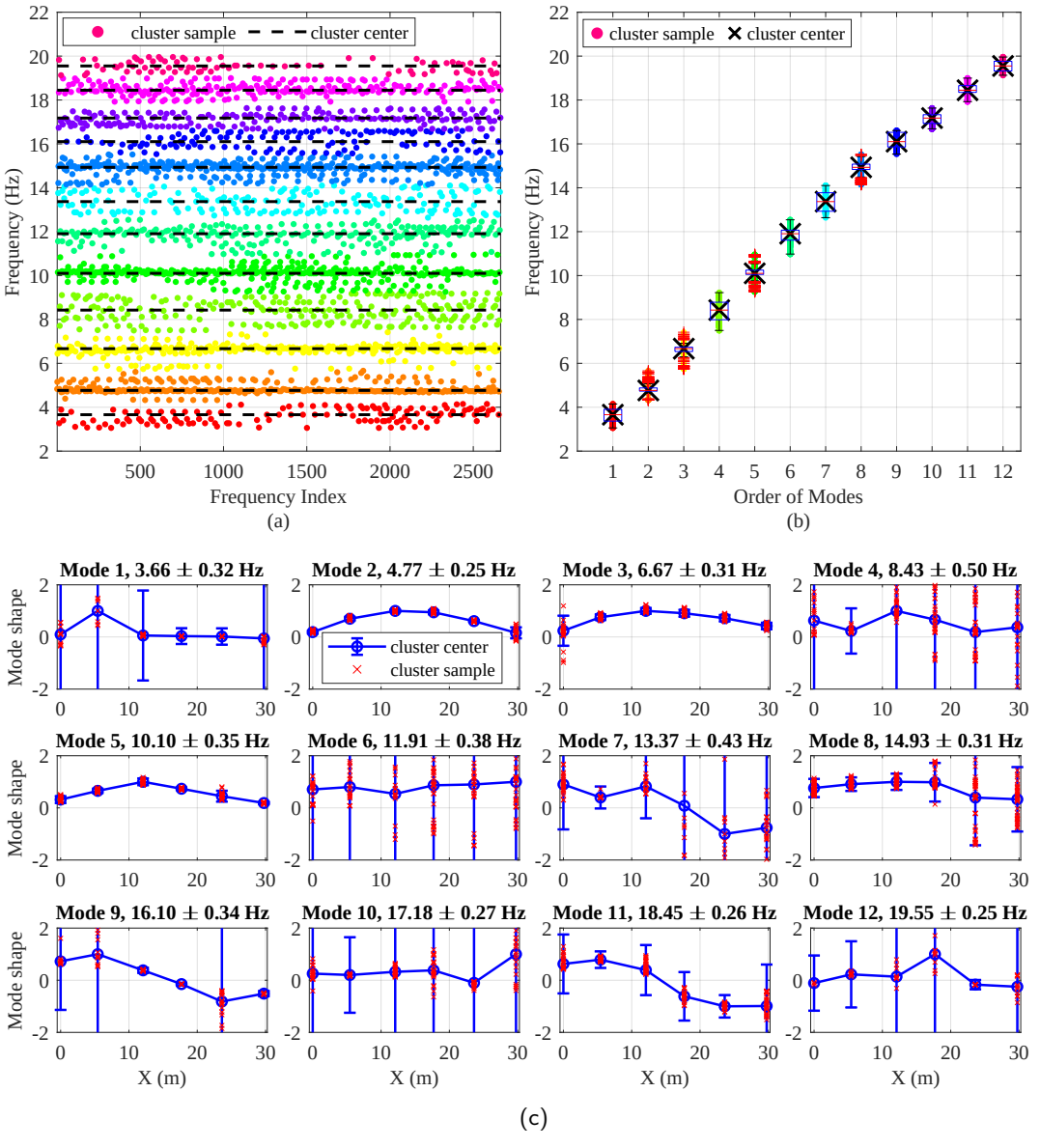

Figure 11: Robust modal identification results for tested bridge span W5: (a) Frequency identification results shown as clusters of frequencies identified from all signal windows. Different clusters are distinguished by colour, with each dot representing a frequency identified from a single signal window. Cluster centres, indicated by dashed lines, represent the median values of the identified frequencies; (b) Box plot of the frequency clusters in (a), used to visualize uncertainty. The median and standard deviation of each frequency cluster is presented in titles of (c); (c) Normalized mode shape identification results. Each red cross indicates the mode shape ratio identified from a single signal window, but some of them exceed the plotting range and are not fully displayed. Crosses are grouped by mode order and sensing location, based on their associated frequencies and satellite-based positioning. The median values of the mode shape ratio clusters at each location are connected by blue lines to visualize the identified mode shapes, with error bars denoting the standard deviation.

with the uncertainty analysis presented in Section 2.2. It is also noteworthy that some lower-order modes in span W5 (e.g., modes 2, 3, and 5) resemble half-sinusoidal waves, which are typically associated only with the first mode of a simply supported beam. Conversely, full sinusoidal waveforms are observed at higher mode orders (e.g., modes 9 and 11), which would ideally correspond to the second mode. This behaviour is reasonable for the tested bridge spans,

which consist of multiple laterally arranged box girders. Further discussion of this phenomenon is provided in the finite element analysis in Section 4.

3.3.3. Population-Level Assessment

This section presents the modal identification results for all 10 tested bridge spans, analysed at the population level to demonstrate the effectiveness of data collection and modal identification. Because identification uncertainty typically increases with mode order, we focus here on the first three identified vibration modes of each span, providing a more reliable basis for comparison.

Figure 12 shows the identified first three modal frequencies for the 10 bridge spans, including their median values and standard deviations. From these results, several key observations emerge:

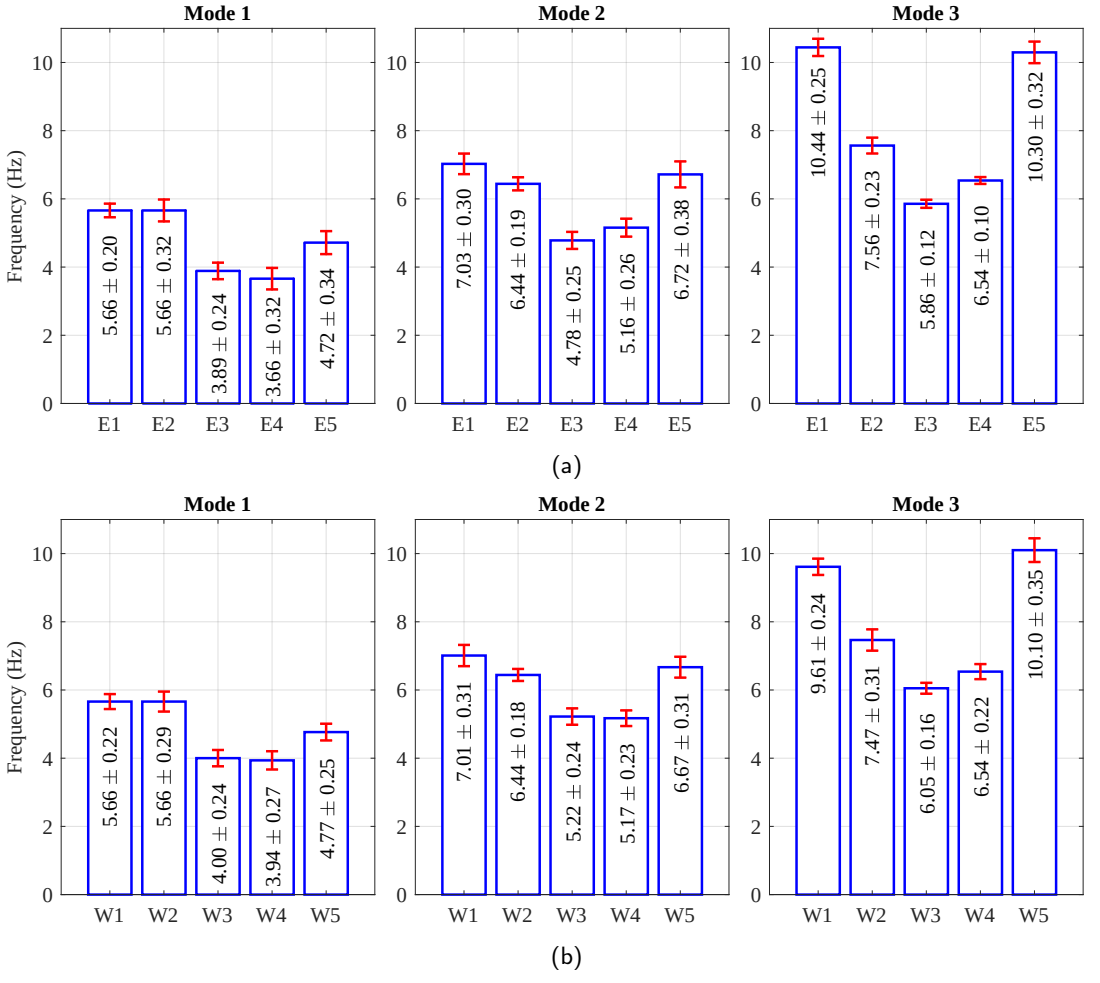

Figure 12: Identified first three modal frequencies with error bars for: (a) Bridge spans E1 to E5; (b) Bridge spans W1 to W5.

1) Similarity across both sides: Although the east-side (E1-E5) and west-side (W1-W5) spans were tested at different times under varying traffic conditions, their identified frequency patterns are remarkably consistent. Specifically, corresponding east and west spans exhibit nearly identical frequencies for each mode. This consistency suggests that the proposed robust modal identification algorithm performs reliably, as these parallel spans share the same length, structural type, as well as material properties, and thus should exhibit similar dynamic characteristics, as validated by the field tests.

2) Dissimilarity within each side: Both Figure 12(a) and (b) reveal that spans 3 and 4 consistently exhibit lower modal frequencies than the other spans. This observation aligns with their longer span lengths (approximately 39 m

for span 3 and 36 m for span 4), which naturally result in higher flexibility and lower modal frequencies. Furthermore, span 3 generally shows slightly lower frequencies than span 4, especially for mode 3, consistent with its greater length.

Among spans 1, 2, and 5, which have similar lengths and widths, the identified frequencies for span 2 are generally lower than those of spans 1 and 5. This difference can be attributed to structural configuration: spans 1 and 5 each contain five box girders arranged laterally, whereas span 2 has only four, resulting in reduced torsional stiffness. This effect is particularly evident in modes 2 and 3, which correspond to torsional modes (as further demonstrated in the finite element analysis in Section 4).

One deviation from theoretical expectation is observed in mode 1. Span 5 exhibits a lower first frequency than spans 1 and 2, despite predictions suggesting the opposite. The cause of this anomaly remains uncertain, as detailed design information for the tested spans is unavailable due to confidentiality constraints.

Figure 12 presents the identified first three mode shapes for the 10 bridge spans. The median identified mode shapes are displayed as lines, with their standard deviations represented by error bars. For reference, the theoretical mode shapes, which are half-sinusoidal waves typical of simply supported beams, are also calculated based on the satellite-derived sensor positions and included as baselines for evaluation. Additionally, the Modal Assurance Criterion (MAC), defined in Equation (14), is employed to quantitatively assess the accuracy of the median identified mode shapes. A MAC value approaching 1 indicates strong agreement between the estimated and theoretical mode shapes. From these results, several key observations can be made:

$$\mathrm{MAC}(\hat{\phi}, \phi) = \frac{\left(\hat{\phi}^{\mathrm{T}}\phi\right)^2}{(\hat{\phi}^{\mathrm{T}}\hat{\phi})(\phi^{\mathrm{T}}\phi)} \tag{14}$$

where $\hat{\phi}$ and ϕ denote the vectors of the identified and theoretical mode shapes, respectively, at all structural nodes.

1) As shown in Figure 12, the MAC values for most median identified mode shapes exceed 0.95, indicating high accuracy in mode shape identification. Additionally, lower accuracy is consistently associated with higher uncertainty, as reflected by larger error bars. This relationship demonstrates that the proposed robust modal identification algorithm provides a reasonable and meaningful evaluation of uncertainty.

2) In general, higher uncertainty is observed near the ends of the identified mode shapes (such as span E2), corresponding to the bridge supports. Furthermore, the uncertainty in the identified mode shapes of the east-side bridge spans is generally lower than that of the west-side spans, due to more consistent and stronger traffic excitation on the east spans. These observations support the theoretical uncertainty analysis, which suggests that identification uncertainty increases as the SNR of the vibration signals decreases.

4. Finite Element Analysis

Though precise details about the dimensions, material properties, and design specifications of the tested bridge spans are unavailable due to confidentiality requirements, we developed a representative finite element model (FEM) using estimated parameters to evaluate the experimental results. The modelling and modal analyses were performed using the widely adopted engineering simulation software ANSYS 2024 R2 [55]. The results are shown in Figure 14.

Figure 14(a) illustrates the constructed FEM, which includes four box girders. Each girder has a height of 2.5 m, a top width of 3.0 m, and a thickness of 2.0 m. The overall bridge model has a length of 30 m and a width of 15 m. To represent structural continuity, diaphragms with a thickness of 0.5 m are modeled at both ends, laterally connecting all box girders. Given that the actual bridge spans are concrete structures, the FEM adopts an elastic modulus of 3.25 GPa and a density of 2500 kg/m^3. The box girders and diaphragms are discretized using `SOLID65` and `SHELL181` elements, respectively, with a mesh size of 0.1 m. Simply supported boundary conditions are applied by constraining all degrees of freedom (DOFs) at one end, while only lateral and vertical DOFs are constrained at the other.

Figures 14(b)-(i) display the modal frequencies and corresponding mode shapes derived from the FEM analysis. Notably, the first three mode shapes along the footpath direction resemble half-sinusoidal waves, which closely match the first three identified mode shapes from field testing (see Figure 13). Higher-order modes, such as the full-sinusoidal shape observed in Figure 14(f), also appear in the field data (e.g., the seventh mode of span E5 shown in Figure 10). Additionally, the FEM-predicted modal frequencies are in reasonable agreement with those measured in the field, despite minor discrepancies arising from the lack of exact design details for high-fidelity modeling. For example, the first three FEM frequencies are 4.03, 6.94, and 11.45 Hz, which are comparable to 4.72, 6.72, and 10.30 Hz for span E5 (shown in Figure 12).

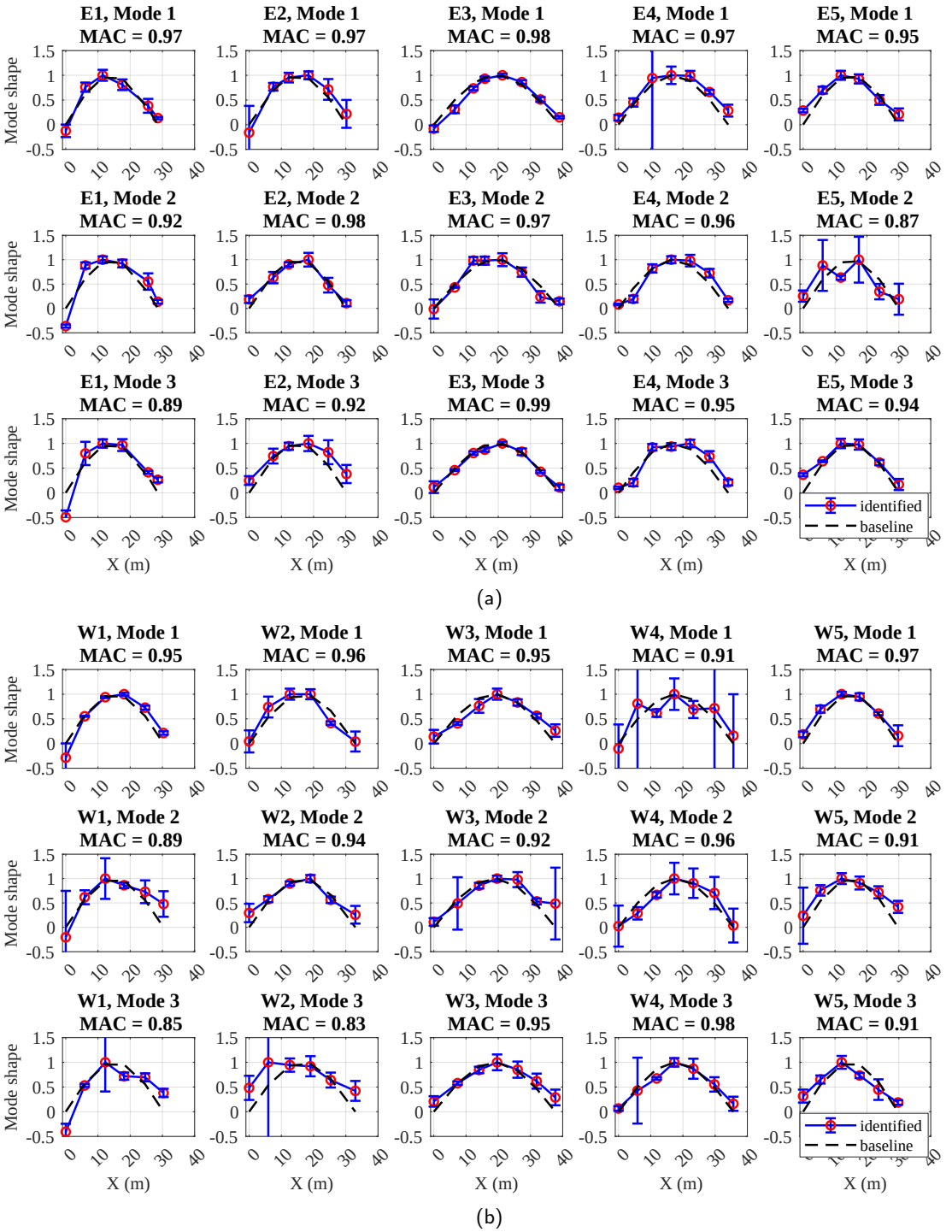

Figure 13: Identified first three mode shapes of: (a) Bridge spans E1 to E5; (b) Bridge spans W1 to W2.

5. Conclusions

This study presents a robotic mobile sensing approach designed to robustly, efficiently, and cost-effectively identify modal frequencies and mode shapes across a population of bridge structures. To this end, we carried out theoretical

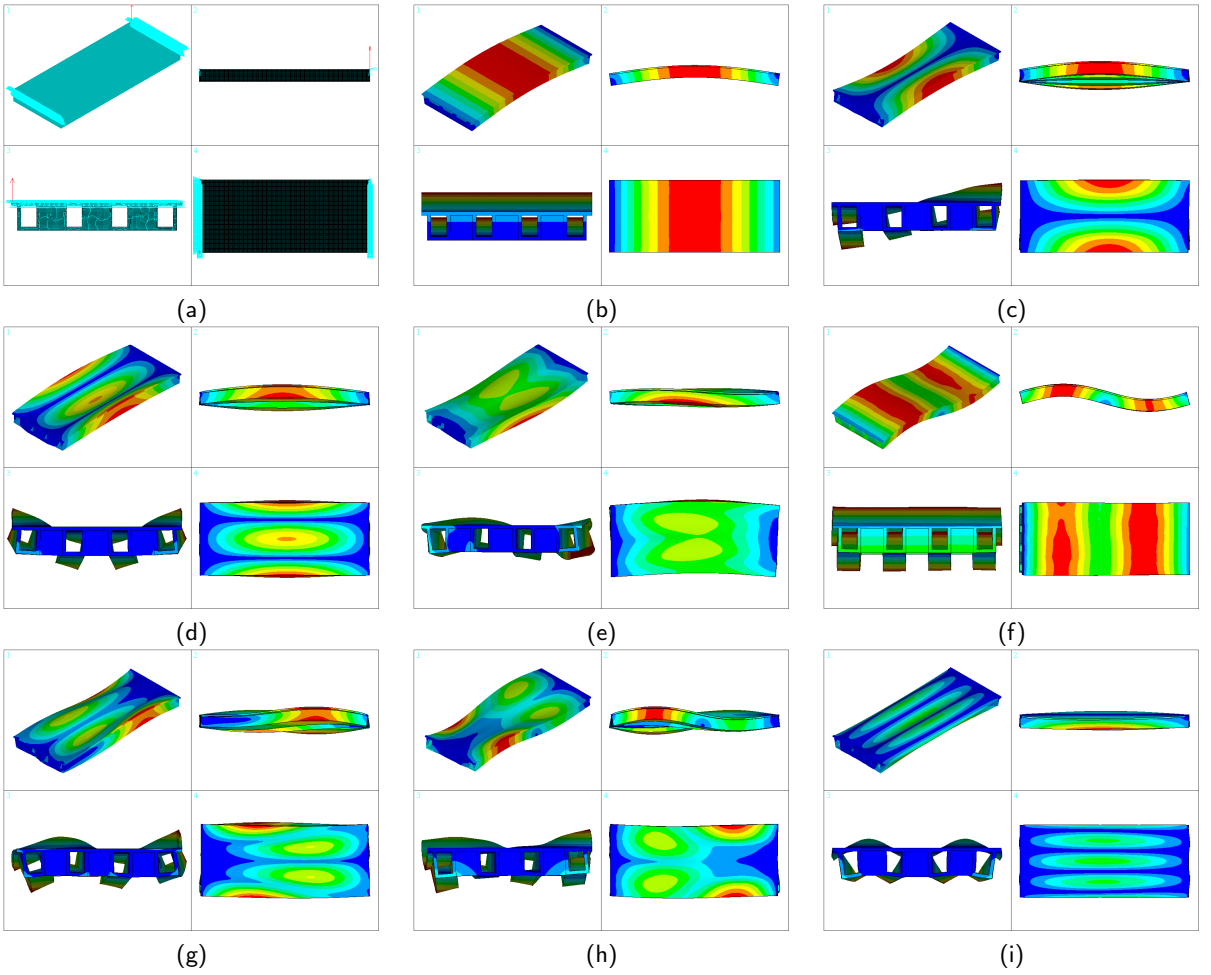

Figure 14: Finite element analysis using ANSYS: (a) Developed finite element model; (b) Mode 1 shape (4.03 Hz); (c) Mode 2 shape (6.94 Hz); (d) Mode 3 shape (11.45 Hz); (e) Mode 4 shape (14.41 Hz); (f) Mode 5 shape (14.45 Hz); (g) Mode 6 shape (17.17 Hz); (h) Mode 7 shape (18.11 Hz); (i) Mode 8 shape (21.15 Hz).

uncertainty analysis, algorithm and hardware development, numerical modelling, and, crucially, field validation on ten bridge spans. The main research findings are summarized as follows:

1) **Uncertainty evaluation**: Both theoretical analysis and field testing show that uncertainty in vibration measurement and modal identification increases under three conditions: i) when the bridge vibration frequency approaches the robot's modal frequency, ii) when the robot is positioned near a node of the bridge mode shape (e.g., at supports for all modes, or at mid-span for higher-order sinusoidal modes), and iii) when bridge excitation is insufficient to generate strong structural responses. The first condition is primarily associated with robot–bridge contact mechanics, while the latter two arise from weak bridge vibration, causing sensor noise to dominate. Although weak excitation is not fully controllable, designing the robot such that its modal frequency is well separated from target bridge modes is recommended to reduce uncertainty.

2) **Practical value**: Field tests on ten bridge spans demonstrate that the proposed robotic mobile sensing approach can effectively and efficiently collect vibration data at the population level. The robust modal identification algorithm successfully identifies modal frequencies and mode shapes, providing both median values and standard deviations to enable uncertainty evaluation. The practical value of the approach is further validated through population-level assessment of the field results and finite element analysis.

3) **Limitations and future research directions**: In this study, the reference sensor was not mounted on a second robot. Implementing this in future work would fully demonstrate the mobility advantages of the proposed approach.

While this study demonstrates feasibility across ten spans, the tested bridge population remains limited in size and variety. Future research should extend the robotic mobile sensing approach to a broader range of bridges in order to build larger, more diverse PBSHM datasets. Finally, this study focuses solely on modal identification. Future work should also explore other PBSHM tasks, such as damage detection, knowledge transfer, and long-term monitoring strategies.

CRediT authorship contribution statement

Xudong Jian: Conceptualization, Methodology, Software, Data curation, Formal analysis, Data visualization, Investigation, Writing - original draft, Writing - Review & Editing. **Kiran Bacsa:** Methodology, Software, Investigation, Writing - Review & Editing. **Matej Varga:** Data curation, Software, Writing - Review & Editing. **Yuguang Fu:** Resources, Writing - Review & Editing. **Eleni Chatzi:** Supervision, Funding Acquisition, Methodology, Resources, Project administration, Writing - Review & Editing.

Declaration of Competing Interest

The authors declare no competing interests exist.

Data Availability Statement

Demonstrative data and codes that implement the proposed robust modal identification algorithm are openly available at our public GitHub repository: https://github.com/JxdEngineer/RobustAFDD. The field test data that support the findings of this study are not publicly available due to privacy restrictions.

Acknowledgments

The research was conducted at the Singapore-ETH Centre, which was established collaboratively between ETH Zurich and the National Research Foundation Singapore. The authors sincerely appreciate the support from the National Research Foundation, Prime Minister's Office, Singapore under its Campus for Research Excellence and Technological Enterprise (CREATE) program. The authors would like to thank Shixing Tian, research intern, for her contributions to the development of the sensing hardware used in this study. We are grateful to Prof. Andreas Wieser, Department of Civil, Environmental and Geomatic Engineering, ETH Zurich, for his guidance on satellite-based positioning. We also sincerely acknowledge the Land Transport Authority of Singapore for their support, which enabled the field validation on real-world bridges.

References

[1] C. Karakostas, G. Quaranta, E. Chatzi, A. C. Zülfikar, O. Çetindemir, G. De Roeck, M. Döhler, M. P. Limongelli, G. Lombaert, N. M. Apaydın, et al., Seismic assessment of bridges through structural health monitoring: a state-of-the-art review, Bulletin of Earthquake Engineering 22 (2024) 1309–1357.

[2] Y. An, E. Chatzi, S.-H. Sim, S. Laflamme, B. Blachowski, J. Ou, Recent progress and future trends on damage identification methods for bridge structures, Structural Control and Health Monitoring 26 (2019) e2416.

[3] D. Anastasopoulos, P. Moretti, T. Geernaert, B. De Pauw, U. Nawrot, G. De Roeck, F. Berghmans, E. Reynders, Identification of modal strains using sub-microstrain fbg data and a novel wavelength-shift detection algorithm, Mechanical Systems and Signal Processing 86 (2017) 58–74.

[4] D. Anastasopoulos, M. De Smedt, L. Vandewalle, G. De Roeck, E. P. Reynders, Damage identification using modal strains identified from operational fiber-optic bragg grating data, Structural Health Monitoring 17 (2018) 1441–1459.

[5] Y. Weng, S.-T. Quek, J. K.-W. Yeoh, Robust vision-based sub-pixel level displacement measurement using a complementary strategy, Mechanical Systems and Signal Processing 223 (2025) 111898.

[6] J. Weng, L. Chen, L. Sun, Y. Zou, Z. Liu, H. Guo, Fully automated and non-contact force identification of bridge cables using microwave remote sensing, Measurement 209 (2023) 112508.

[7] J. P. Lynch, K. J. Loh, A summary review of wireless sensors and sensor networks for structural health monitoring, Shock and Vibration Digest 38 (2006) 91–130.

[8] J. Seo, L. Duque, J. Wacker, Drone-enabled bridge inspection methodology and application, Automation in construction 94 (2018) 112–126.

[9] V. Hoskere, J.-W. Park, H. Yoon, B. F. Spencer Jr, Vision-based modal survey of civil infrastructure using unmanned aerial vehicles, Journal of Structural Engineering 145 (2019) 04019062.

[10] Y. Narazaki, V. Hoskere, G. Chowdhary, B. F. Spencer Jr, Vision-based navigation planning for autonomous post-earthquake inspection of reinforced concrete railway viaducts using unmanned aerial vehicles, Automation in Construction 137 (2022) 104214.

[11] C. Stoura, V. K. Dertimanis, E. Chatzi, Drive-by modal identification of railway bridges via on-board measurements from a single railroad vehicle, in: Proceedings of the 11th European Workshop on Structural Health Monitoring (EWSHM 2024), volume 29, NDT. net, 2024, p. 482.
[12] C. D. Stoura, V. K. Dertimanis, E. N. Chatzi, Identification of railway bridge modal properties via acceleration data from traversing trains, in: IMAC, A Conference and Exposition on Structural Dynamics, Springer, 2024, pp. 83–89.
[13] H. M. Siu, F. Filippitzis, C. D. Stoura, C. Papadimitriou, E. G. Dimitrakopoulos, Utilizing on-board sensing of passing train vehicles for virtual sensing of bridges, Engineering Structures 319 (2024) 118808.
[14] X. Jian, Y. Xia, L. Sun, An indirect method for bridge mode shapes identification based on wavelet analysis, Structural Control and Health Monitoring 27 (2020) e2630.
[15] X. Jian, Y. Xia, L. Sun, Indirect identification of bridge frequencies using a four-wheel vehicle: Theory and three-dimensional simulation, Mechanical Systems and Signal Processing 177 (2022) 109155.
[16] Q. Mei, M. Gül, M. Boay, Indirect health monitoring of bridges using mel-frequency cepstral coefficients and principal component analysis, Mechanical Systems and Signal Processing 119 (2019) 523–546.
[17] K. Gkoktsi, F. Bono, D. Tirelli, Effectiveness of drive-by monitoring in short-span bridges: A real-scale experimental evaluation, Structural Control and Health Monitoring 2024 (2024) 3509941.
[18] L. Cronin, D. Sen, G. Marasco, I. Dabbaghchian, L. Benedetti, T. Matarazzo, S. Pakzad, A roadmap for ubiquitous crowdsourced mobile sensing-based bridge modal identification, Sensors 25 (2025) 2528.
[19] D. Zhu, J. Guo, C. Cho, Y. Wang, K.-M. Lee, Wireless mobile sensor network for the system identification of a space frame bridge, Ieee/Asme Transactions On Mechatronics 17 (2012) 499–507.
[20] X. Jian, Z. Lai, K. Bacsa, Y. Fu, C. G. Koh, L. Sun, A. Wieser, E. Chatzi, A robotic automated solution for operational modal analysis of bridges with high-resolution mode shape recovery, Journal of Structural Engineering 150 (2024) 04024081.
[21] L. Ge, A. Sadhu, Deep learning-enhanced smart ground robotic system for automated structural damage inspection and mapping, Automation in Construction 170 (2025) 105951.
[22] F. Luleci, A. Algadi, Z. Li, F. N. Catbas, Robot-based bridge indirect monitoring leveraging road data filtering for modal frequency estimation, Structure and Infrastructure Engineering 0 (2025) 1–23.
[23] T. Panigati, M. Zini, D. Striccoli, P. F. Giordano, D. Tonelli, M. P. Limongelli, D. Zonta, Drone-based bridge inspections: Current practices and future directions, Automation in Construction 173 (2025) 106101.
[24] A. Kamariotis, E. Chatzi, D. Straub, Value of information from vibration-based structural health monitoring extracted via bayesian model updating, Mechanical Systems and Signal Processing 166 (2022) 108465.
[25] A. Cicirello, Physics-enhanced machine learning: a position paper for dynamical systems investigations, arXiv preprint arXiv:2405.05987 (2024).
[26] M. Haywood-Alexander, W. Liu, K. Bacsa, Z. Lai, E. Chatzi, Discussing the spectra of physics-enhanced machine learning via a survey on structural mechanics applications, arXiv preprint arXiv:2310.20425 (2023).
[27] K. Worden, L. A. Bull, P. Gardner, J. Gosliga, T. J. Rogers, E. J. Cross, E. Papatheou, W. Lin, N. Dervilis, A brief introduction to recent developments in population-based structural health monitoring, Frontiers in Built Environment 6 (2020).
[28] L. A. Bull, P. A. Gardner, J. Gosliga, T. J. Rogers, N. Dervilis, E. J. Cross, E. Papatheou, A. Maguire, C. Campos, K. Worden, Foundations of population-based shm, part i: Homogeneous populations and forms, Mechanical systems and signal processing 148 (2021) 107141.
[29] P. Gardner, L. Bull, J. Gosliga, N. Dervilis, K. Worden, Foundations of population-based shm, part iii: Heterogeneous populations–mapping and transfer, Mechanical Systems and Signal Processing 149 (2021) 107142.
[30] J. Gosliga, P. Gardner, L. Bull, N. Dervilis, K. Worden, Foundations of population-based shm, part ii: Heterogeneous populations–graphs, networks, and communities, Mechanical systems and signal processing 148 (2021) 107144.
[31] G. Tsialiamanis, C. Mylonas, E. Chatzi, N. Dervilis, D. J. Wagg, K. Worden, Foundations of population-based shm, part iv: The geometry of spaces of structures and their feature spaces, Mechanical Systems and Signal Processing 157 (2021) 107692.
[32] V. Giglioni, J. Poole, R. Mills, I. Venanzi, F. Ubertini, K. Worden, Transfer learning in bridge monitoring: Laboratory study on domain adaptation for population-based shm of multispan continuous girder bridges, Mechanical Systems and Signal Processing 224 (2025) 112151.
[33] A. J. Ferguson, D. Hester, F. Huseynov, C.-W. Kim, J. Brownjohn, R. Woods, L. A. Bull, On the normalisation and mapping of influence lines, Mechanical Systems and Signal Processing 237 (2025) 112883.
[34] L. Ge, A. Sadhu, Domain adaptation for structural health monitoring via physics-informed and self-attention-enhanced generative adversarial learning, Mechanical Systems and Signal Processing 211 (2024) 111236.
[35] G. Delo, R. Roy, K. Worden, C. Surace, On the use of the inverse finite element method to enhance knowledge sharing in population-based structural health monitoring, Computers & Structures 307 (2025) 107635.
[36] A. Bunce, D. S. Brennan, A. Ferguson, C. O'Higgins, S. Taylor, E. J. Cross, K. Worden, J. Brownjohn, D. Hester, On population-based structural health monitoring for bridges: Comparing similarity metrics and dynamic responses between sets of bridges, Mechanical Systems and Signal Processing 216 (2024) 111501.
[37] X. Jian, Y. Xia, G. Duthé, K. Bacsa, W. Liu, E. Chatzi, Using graph neural networks and frequency domain data for automated operational modal analysis of populations of structures, Data-Centric Engineering 6 (2025) e45.
[38] X. Jian, K. Bacsa, G. Duthé, E. Chatzi, Modal decomposition and identification for a population of structures using physics-informed graph neural networks and transformers, arXiv preprint arXiv:2505.04018 (2025).
[39] G. Tsialiamanis, C. Sbarufatti, N. Dervilis, K. Worden, On a meta-learning population-based approach to damage prognosis, Mechanical Systems and Signal Processing 209 (2024) 111119.
[40] D. S. Brennan, J. Gosliga, E. J. Cross, K. Worden, Foundations of population-based shm, part v: Network, framework and database, Mechanical Systems and Signal Processing 223 (2025) 111602.

[41] F. Gong, W. Luo, T. He, Y. Xia, Time-varying damping ratio identification for structures subjected to traffic loads using signal stabilization technique, Mechanical Systems and Signal Processing 232 (2025) 112715.
[42] S. Greś, M. Döhler, L. Mevel, Uncertainty quantification of the modal assurance criterion in operational modal analysis, Mechanical Systems and Signal Processing 152 (2021) 107457.
[43] S. Greś, M. Döhler, P. Andersen, L. Mevel, Uncertainty quantification for the modal phase collinearity of complex mode shapes, Mechanical Systems and Signal Processing 152 (2021) 107436.
[44] H. Kυ, Notes on the use of propagation of error formulas, Journal of Research of the National Bureau of Standards: Engineering and instrumentation. Section C. 70 (1966) 263.
[45] E. Cheynet, J. B. Jakobsen, J. Snæbjörnsson, Damping estimation of large wind-sensitive structures, Procedia engineering 199 (2017) 2047–2053.
[46] R. Brincker, L. Zhang, P. Andersen, Modal identification from ambient responses using frequency domain decomposition, in: IMAC 18: Proceedings of the International Modal Analysis Conference (IMAC), San Antonio, Texas, USA, February 7-10, 2000, 2000, pp. 625–630.
[47] DJI, RoboMaster EP, DJI, 2022. URL: https://www.dji.com/sg/robomaster-ep.
[48] Xsens, Xsens MTi-680G, 2023. URL: https://www.xsens.com/hubfs/Downloads/Leaflets/MTi-680G.pdf.
[49] Raspberry Pi Foundation, Raspberry Pi 5, 2025. URL: https://datasheets.raspberrypi.com/rpi5/raspberry-pi-5-product-brief.pdf.
[50] Analog Devices Inc., ADXL 355, 2025. URL: https://www.analog.com/media/en/technical-documentation/data-sheets/adxl354_adxl355.pdf.
[51] u-blox, ZED-F9P, 2023. URL: https://www.mouser.sg/datasheet/2/1025/ZED_F9P_01B_DataSheet_UBX_17051259-3180183.pdf.
[52] R. K. Pearson, Y. Neuvo, J. Astola, M. Gabbouj, Generalized hampel filters, EURASIP Journal on Advances in Signal Processing 2016 (2016) 1–18.
[53] The MathWorks, Inc., MATLAB Version R2024b, Natick, Massachusetts, United States, 2024. URL: https://www.mathworks.com/products/matlab.html.
[54] X. Jian, GitHub repository, 2025. https://github.com/JxdEngineer/RobustAFDD.
[55] ANSYS, Inc., ANSYS® Release 2024 R2, Canonsburg, Pennsylvania, USA, 2024. URL: https://www.ansys.com.